Economic Geology, v. 108, pp. 987–1013

The Metal Content of Silicate Melts and Aqueous Fluids in Subeconomically Mo Mineralized Granites: Implications for Porphyry Mo Genesis

Linda Lerchbaumer† and Andreas Audétat

Bayerisches Geoinstitut, Universität Bayreuth, 95440 Bayreuth

Abstract

To better understand the factors leading to porphyry Mo mineralization, we studied melt and fluid inclusions in three subeconomically Mo mineralized granites in well-known Mo provinces: the Treasure Mountain dome in the Colorado mineral belt (USA), and the Drammen and Glitrevann granites in the Oslo rift (Norway). Melt and fluid inclusions were investigated in samples ranging from coarsely crystallized whole rocks to euhedral quartz crystals within miarolitic cavities. The major and trace element chemistry of individual inclusions was determined by laser ablation-inductively coupled plasma-mass spectrometry. Melt inclusions are rhyolitic in composition and record a clear trend of increasing Mo concentrations with increasing degree of melt differentiation as monitored by Cs, extending from ~5 to 10 ppm Mo at 5 ppm Cs to ~17 to 40 ppm Mo at 100 ppm Cs. Coexisting magmatic fluids were single phase, had a salinity of 4 to 6 wt % NaCl equiv and a density of 0.6 to 0.7 g/cm^3, and contained ~0.5 wt % S and up to 6 mol % CO_2. Molybdenum concentrations in these fluids ranged from ~20 to ~200 ppm Mo, except for some highly evolved fluids that had lower Mo contents.

Comparison of our data with published fluid and melt inclusion data from porphyry Mo deposits, porphyry Cu (Mo, Au) deposits, and barren intrusions reveals that most subduction-related magmas have lower Mo/Cs ratios than within-plate magmas, but that within these two groups there are no systematic differences between barren and productive intrusions. This suggests that the mineralization potential was not primarily controlled by the metal content of the melts and fluids, but rather by other factors such as size of the magma chamber and the efficiency of residual melt and fluid extraction from the magma chamber and their focusing into a small apophysis at its top. Based on our data, it can be calculated that at least several tens of km^3 of magma were necessary to form intermediate-sized Mo deposits, and at least several hundred km^3 to form giant (≥1 Mt Mo) deposits. All three granites investigated in this study would have been large enough to produce at least an intermediate-sized Mo deposit, but they nevertheless are only subeconomically mineralized. Their low productivity thus appears to be the result of poor fluid focusing. Factors promoting a high degree of fluid focusing include (1) accumulation of major volumes of fractionated, crystal-poor melts at the top of the magma chamber, (2) formation of an apophysis, and (3) development of convection cells, leading to an efficient circulation of these fractionated melts through the apophysis.

Introduction

Molybdenum, a sought-after alloying metal due to its high-strength properties and very high melting point, is principally mined from porphyry-type ore deposits. About half of the production stems from porphyry Mo deposits, in which this metal is the principal commodity (i.e., Mo/Cu >1), and the other half from porphyry Cu (Mo, Au) deposits, in which Mo is recovered as a valuable by-product (e.g., Carten et al., 1993). This study focuses on the formation of the former type of deposits and, more specifically, on the subclass of Climax-type deposits, which are associated with highly evolved, rift-related rhyolites, as opposed to the subclass of low-grade, arc-related deposits that are associated with less evolved, calc-alkaline magmas (Westra and Keith, 1981; Carten et al., 1993). Up to now, by far the largest producers of the Climax type were Climax (Colorado, USA), Urad-Henderson (Colorado, USA), and Questa (New Mexico, USA), which have provided nearly 80% of the Mo mined from porphyry Mo deposits (Mutschler et al., 1999). Although many porphyry Mo occurrences have been thoroughly investigated with respect to their geologic setting, intrusion sequence, petrography, wall-rock alteration, and ore distribution, only little data exist concerning the metal content of the silicate melts and the magmatic-hydrothermal fluids that were responsible for the transport and deposition of Mo. One of the main reasons for this paucity of data is the difficulty of finding analyzable fluid and melt inclusions, which appears to reflect unfavorable formation conditions combined with a high percentage of subsequent inclusion destruction in this type of ore deposits. So far, larger data sets have been available only from two occurrences: the porphyry Mo deposit at Questa, New Mexico (Klemm et al., 2008; only fluid inclusion data), and the porphyry Mo (Nb) deposit at Cave Peak, Texas (Audétat, 2010; both fluid and melt inclusion data). Additionally, limited melt inclusion data are available from Pine Grove, Utah (Lowenstern, 1994; Audétat et al., 2011), and from the Henderson-related Hideaway Park ignimbrite (USGS Denver Inclusion Analysis Laboratory, http://minerals.cr.usgs.gov/dial/Henderson_Mo.html).

The studies on Cave Peak and Questa returned rather contrasting values for metal contents in magmatic bulk fluids: at Cave Peak, intermediate-density fluid inclusions coexisting with highly fractionated melt inclusions contain ~100 ppm Mo and ~600 ppm Cu (i.e., Mo/Cu ~0.2), whereas at Questa, pre-mineralization, intermediate-density fluid inclusions trapped in quartz of a magmatic-hydrothermal breccia contain ~40 ppm Mo and ~3,000 ppm Cu (i.e., Mo/Cu ~0.01). Particularly in the latter case, the high Cu concentrations are unexpected, given the fact that the deposit does not contain any recoverable copper.

† Corresponding author: e-mail, lindaler@yahoo.de

Submitted: May 11, 2012
Accepted: October 18, 2012

To get a better overview of the composition of Mo-mineralizing melts and fluids, we investigated samples from three subeconomically Mo mineralized intrusions. As was mentioned above, analyzable fluid and melt inclusions are rather rare in intrusions associated with economic Mo deposits; hence, we focused on small, subeconomic occurrences that contain well-preserved inclusions, noting that the difference between economic and subeconomic occurrences does not necessarily lie in the composition of the melts and fluids, but may be due to other parameters, such as the size of the magma chamber and the degree of fluid focusing. The two main questions addressed in this study are, (1) What are typical metal concentrations in Mo-mineralizing fluids and melts?, and (2) What factors determine the Mo-mineralizing potential of granitic intrusions?

Samples

Samples were collected from granitic intrusions in two areas that are well known for granite-related Mo mineralization: the Colorado mineral belt (USA) and the Oslo rift (Norway).

Treasure Mountain dome (Colorado, USA)

The Treasure Mountain dome is a large, granitic intrusion in the central part of the Colorado mineral belt, which hosts some of the world's biggest porphyry Mo deposits, including the famous Climax and Urad-Henderson orebodies (Fig. 1). The Colorado mineral belt is an NE-trending belt of about 400-km length and 20- to 60-km width. The belt hosts numerous Au, Ag, Cu, Mo, Pb, and Zn deposits. Most of these deposits are genetically associated with monzonitic to granitic intrusions of Laramide (~70–80 to 35–55 Ma) age (Tweto and Sims, 1963; Bookstrom, 1989), whereas all porphyry Mo deposits are of Oligocene (23–34 Ma) to Pliocene (5.3–2.6 Ma) age (e.g., White et al., 1981; Wareham et al., 1998). Minor Mo mineralization occurring in pegmatitic segregations or as local disseminations within the Precambrian basement is related to igneous activity at 1.7., 1.4, and 1.0 Ga (Lehmann, 1987).

The Colorado mineral belt coincides with a large-scale negative Bouguer anomaly (Fig. 1) that reflects primarily Laramide-age intrusions emplaced along a reactivated Precambrian shear zone. However, local negative Bouguer

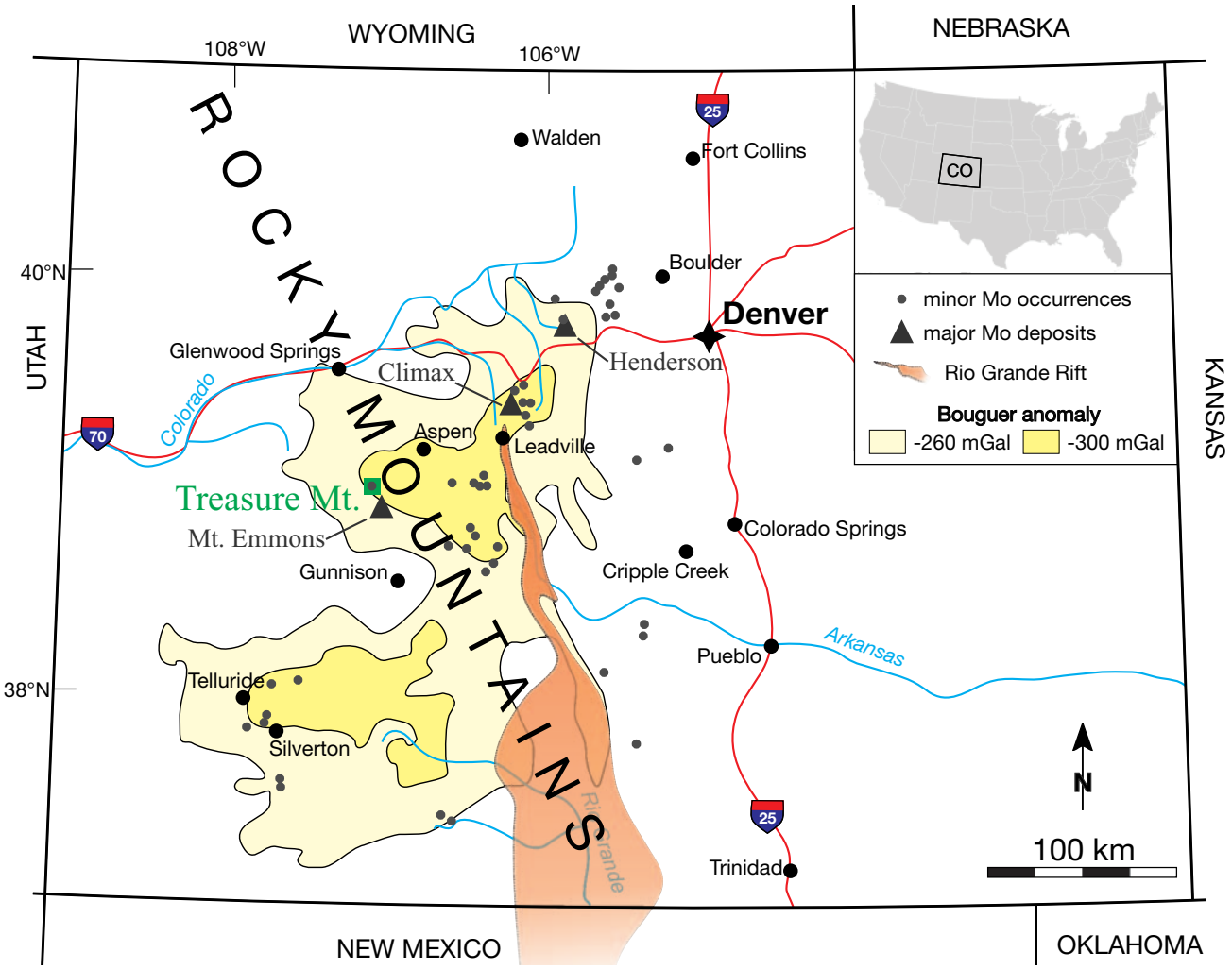

FIG. 1. Sketch map of Colorado showing the location of major and minor Mo deposits and occurrences (Lehmann, 1987) relative to an underlying batholith indicated by Bouguer anomaly-minima (http://pubs.usgs.gov/of/2000/ofr-00-0042/colo_boug.htm) and the Rio Grande rift (dimensions from White et al., 1981). The boundaries of the Colorado mineral belt more or less coincide with the outer limits of the –260 mGal anomaly.

anomalies are spatially associated with the porphyry Mo deposits and are interpreted to reflect large leucogranite bodies that were emplaced in the Oligocene to Pliocene, i.e., more than 10 m.y. after subduction-related magmatism in the Laramide period stopped, but coinciding with the initiation of the Rio Grande rift (White et al., 1981; Bookstrom, 1989). A fundamental change in the mode of magmatism is also evident in the major and trace element chemistry of the magmas. Laramide-age magmas cover the entire suite from monzonitic to granitic compositions and show a clearly subduction related, calc-alkaline character, whereas magmas associated with porphyry Mo mineralization are strongly bimodal (high-silica rhyolites coexisting with minor lamprophyres; Bookstrom et al., 1988), distinctly potassic, and of A-type (i.e., intraplate) affinity (e.g., White et al. 1981; Carten et al., 1993; USGS Denver Inclusion Analysis Laboratory, http://minerals.cr.usgs.gov/dial/Henderson_Mo.html).

The Treasure Mountain dome, located about 10 km southeast of the town of Marble, has been dated at an age of 12.4 ± 0.6 Ma (Obradovich et al., 1969). It shares many similarities with the Oligocene (23–34 Ma) Climax-Alma batholith ~90 km to the northeast, the apophyses of which produced the Climax and Urad-Henderson deposits (Bookstrom, 1989). Forceful intrusion of granitic magma into Paleozoic sedimentary rocks at Treasure Mountain formed a dome that measures 15 km in length, 12 km in width, and ~1.4 km in height (Mutschler, 1976). The crest of the intrusion is exposed at an altitude of ~3,880 m, close to the top of Treasure Mountain. In this area, molybdenite-bearing veins and disseminations within the granite and in the overlying Precambrian basement are common. Vein-type mineralization is represented by small, widely spaced quartz-sericite-pyrite-fluorite veins containing minor molybdenite, whereas disseminations are represented by quartz-pyrite-sericite-orthoclase-fluorite-tourmaline-molybdenite greisens (Mutschler, 1976). Small pegmatitic veins and miarolitic cavities filled with quartz, orthoclase, pyrite, and fluorite are also common.

Four different granite facies have been distinguished by Mutschler (1976): (1) a medium- to coarse-grained, equigranular to slightly porphyritic facies that occurs only at intermediate to low elevations ("Granular facies"), (2) a porphyritic facies with 60 to 90 vol % phenocrysts of quartz and K-feldspar set in a fine-grained matrix, forming an up to 200-m-thick sheet above the granular facies ("Twin Bridges porphyry facies"), (2) a leucocratic porphyry facies containing 20 to 50 vol % phenocrysts of quartz, K-feldspar, and plagioclase set in a very fine grained matrix, forming an up to 10-m-thick border phase in the apical part of the intrusion ("Bear Mountain porphyry phase"), and (4) an even more leucocratic porphyry phase containing small phenocrysts of quartz, K-feldspar, and albite in an extremely fine grained matrix, occurring as dikes intruded into Paleozoic and Mesozoic sediments along the flanks of the dome ("White Quartz porphyry phase"). Whole-rock analyses reported in Mutschler et al. (1976) range from 75 wt % SiO_2 in the granular facies to 80 wt % SiO_2 in aplite veins (normalized to 100% volatile-free), and are all subaluminous to mildly peraluminous with A/CMK (= molar $Al_2O_3/(CaO + Na_2O + K_2O)$) between 1.0 and 1.1. Samples were taken from the granular facies at an elevation of 3,580 m (sample TM 2; coordinates 39°01'45.2"N, 107°06'26.4"W; WGS84 datum), from the leucocratic Bear Mountain porphyry border phase (hereafter simply called "border phase") at an elevation of 3,870 m (sample TM 7; 39°01'15.7"N, 107°06'40.2"W), and from three miarolitic cavities (samples TM 5, TM 10, TM 12) in the vicinity of the latter sample, all hosted by the border phase. The miarolitic cavities measured 5 to 15 cm in diameter and were lined with euhedral crystals of quartz and orthoclase ± fluorite.

Drammen granite (Norway)

The Drammen granite is a composite granitic body in the central part of the Oslo rift (Fig. 2), which formed during Permo-Carboniferous rifting in northern Europe. The various occurrences of Mo (and Fe, Mn, Ti, W, Mb, Zn, Pb, Cu, Bi) mineralization in the Oslo region stem from this rift-related, subalkaline magmatism (Schønwandt and Petersen, 1983). Thus, all Mo occurrences of the Oslo rift belong to the

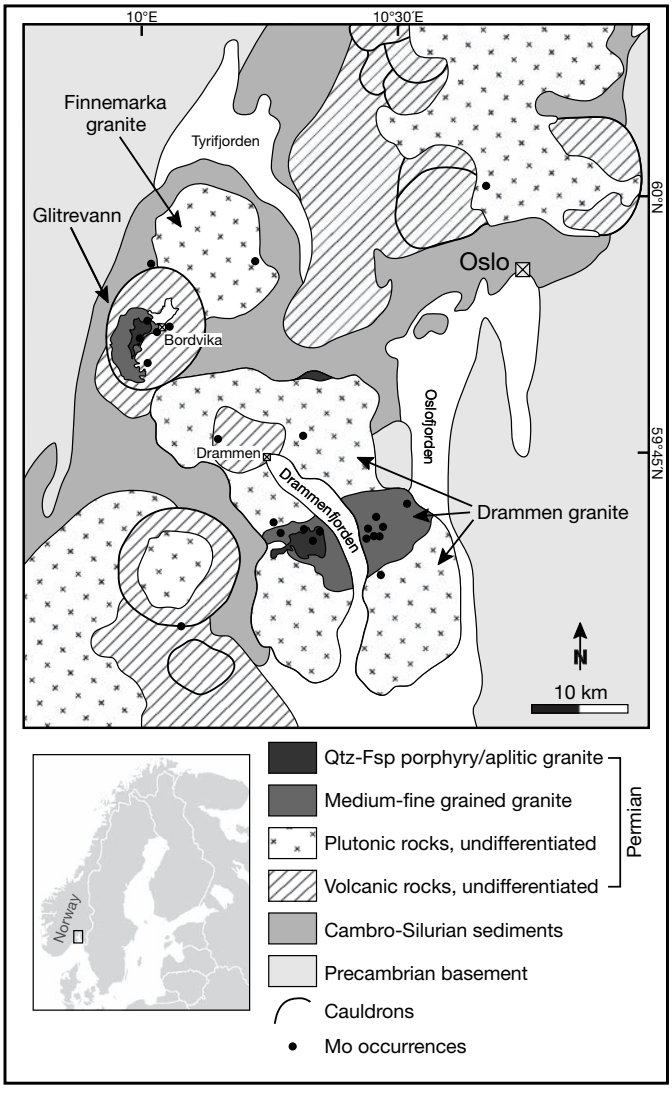

FIG. 2. Sketch map of the Glitrevann and Drammen granites in the central Oslo rift, showing the rock types discussed in this work (modified after Ihlen et al., 1982; Schønwandt and Petersen, 1983; Schønwandt, 1986). The "Qtz-Fsp (quartz-feldspar) porphyry/aplitic granite" phase within the Glitrevann granite corresponds to the extent of the aplitic granite (see text for details).

alkalic type described by Carten et al. (1993). Although numerous, none of the Mo mineralizations are regarded as exploitable (Ihlen, 1986).

The geologic history of the Oslo region goes back to the Proterozoic, when the basement rocks formed and subsequently were metamorphosed in the Sveconorwegian orogeny (1200–900 Ma) (e.g., Berthelsen, 1980; Skjernaa and Pedersen, 1982). Faulting of these gneisses, metagabbros, metasediments, and migmatites started some 970 m.y. ago and continued intermittently until post-Permian times (Starmer, 1972, 1985a, b). The present Oslo rift formed in the period of 305 to 240 Ma (e.g., Sundvoll and Larsen, 1990). The Oslo graben, which is the main rift structure exposed on land, extends north-northeast with a total length of 400 km. Within this graben, Paleozoic sedimentary and magmatic rocks are preserved, whereas the areas to the east and west consist of Precambrian metamorphic rocks. Erosion stripped away parts of the volcanic rocks, exposing underlying intrusive rocks and structures (Neumann et al., 1992). The earliest magmatic activity in the rift is represented by syenitic and mafic sills dated at 304 to 294 Ma (Sundvoll and Larsen, 1982; Sundvoll et al., 1992). During the main phase of rifting, large volumes of "rhomb porphyry" lavas interlayered with basalts were erupted (Ramberg et al., 1977). Rifting terminated with the formation of central volcanoes along preexisting fractures and faults, and the magmatic style changed from basaltic extrusions to intrusion of composite batholiths of intermediate to granitic compositions at 275 to 240 Ma (Neumann et al., 1992).

The largest of these granitic bodies is the Drammen granite, a complex of polyphase intrusions of biotite-granites and porphyries dated at 270 to 278 Ma by Rb-Sr chronology (Sundvoll and Larsen, 1990). Ihlen et al. (1982) subdivided the granitic rocks of the intrusion into eight textural facies, which all grade into each other. Because molybdenite mineralization is confined to the "medium- to fine-grained, partly porphyritic granite" and the "quartz-feldspar porphyries with aplitic to microcrystalline groundmass" as defined by Ihlen et al. (1982), only these two rock types will be discussed in further detail. The first facies (herein called "medium- to fine-grained granite") comprises an area of 60 to 70 km² on both sides of the Drammen fjord in the central part of the complex (Fig. 2). The average grain size of this rock is 1 to 3 mm, with some samples displaying a porphyritic texture. High contents of quartz and plagioclase, plus the appearance of muscovite and fresh or slightly chloritized biotite are typical features. The second facies (herein called "quartz-feldspar porphyry") occurs at the western edge of the medium- to fine-grained granite (Fig. 2). This facies contains 2- to 4-mm-sized phenocrysts of quartz, alkali-feldspar, and plagioclase embedded in a reddish, microcrystalline groundmass (Ihlen et al., 1982). Both facies contain between 76.3 and 78.9 wt % SiO_2 and are mildly peraluminous with A/CNK values of 1.05 to 1.13 (Ihlen et al., 1982; Trønnes and Brandon, 1992).

Mineralization occurs as (1) quartz-fluorite-molybdenite-veins and disseminations of molybdenite ± wolframite within the surrounding granite, and (2) as contact metasomatic deposits of Fe-Cu-Zn-Pb-Bi ± Mo within surrounding metasedimentary and metavolcanic rocks (e.g., Bugge, 1963; Ihlen and Vokes, 1978; Ihlen et al., 1982).

The samples described in this study were collected from the medium- to fine-grained granite on the eastern shore of the Drammen Ffjord, a few hundred meters east of Grimsrudbukta (~59°41'06"N, 10°25'58"E). Sample Dra 2 is a miarolitic cavity of ~10-cm size that was hosted by a local segregation of aplite, whereas samples Dra 6 and Dra 20 are similar-sized miarolitic cavities that were hosted by medium-grained granite. All cavities contained euhedral crystals of smoky quartz, orthoclase, albite, and white mica.

Glitrevann granite (Norway)

The Glitrevann caldera is the northernmost of a prominent N-S trending array of calderas west of the Drammen granite (Fig. 2), featuring porphyry-style molybdenum mineralization in subvolcanic rocks (Geyti and Schønwandt, 1979). The Glitrevann caldera cuts the Finnemarka granite and is, in turn, cut by the Drammen granite. Thus, the age of the Drammen granite marks the upper limit for caldera formation (Schønwandt and Petersen, 1983). The Glitrevann complex consists of a central granitic stock surrounded by a syenitic ring complex and Permian lavas (Oftedahl, 1953). An overview of the evolution of the structure is given by Schønwandt and Petersen (1983): It started with the eruption of rhyolitic dome complexes and ignimbrites associated with basaltic volcanism. Eruption of voluminous ash flows in the southern sector then caused collapse and formation of the semicircular Glitrevann caldera. Within this central caldera, meso- and megabreccias, as well as rhyolitic ash flows, are preserved. The northern part of the caldera was flooded simultaneously by rhomb porphyry flows, basaltic lava, and ash tuffs. The final events were the eruption of the Bordvika ignimbrite, intrusion of syenitic ring dikes, and the emplacement of a central, composite granite stock, which caused uplift of the caldera.

The central granitic stock can be subdivided into three types: medium-grained granite, porphyritic granite, and aplitic granite (Jensen, 1985), with the latter hosting the majority of mineralization (Schønwandt and Petersen, 1983). Based on cross-cutting relationships and trace element abundances, it is clear that aplitic granite is the youngest phase (Jensen, 1985). The aplitic granite occupies ca. 20% of the outcrop area and is made up of a fine-grained intergrowth of quartz and alkali feldspar containing few feldspar, quartz, and biotite phenocrysts. Due to its compositional similarity with the quartz-feldspar porphyry, these two rock types are not distinguished in Figure 2. Aplitic granite contains between 76.2 and 77.6 wt % SiO_2 and has A/CNK and A/NK ratios of 0.94 to 0.99 and 0.98 to 1.04, respectively, and is therefore classified as mildly peralkaline to mildly metaluminous (Jensen, 1985).

Molybdenum mineralization within the granitic stock is manifold (Schønwandt, 1986) and occurs (1) as disseminations in pervasively sericite altered host rocks, (2) in the aplite granite in open fractures together with quartz and pyrite, (3) in quartz-alkali feldspar pegmatites, and (4) in miarolitic cavities together with pyrite, quartz, and alkali feldspar. In the central part of the caldera, where the Bordvika ignimbrite covers the aplitic zone in the form of a massive, impermeable cap rock, the mineralization forms a stockwork of quartz-molybdenite veins enveloped by sericitic alteration (Geyti and Schønwandt, 1979).

Samples were taken from two miarolitic cavities hosted by aplitic granite on the southern shore of Lake Sandungen (59°51'06"N, 10°02'29"E). The cavities measured 5 to 10 cm in diameter and were lined with quartz and orthoclase.

Methods

Doubly polished thick sections of 0.1- to 1.0-mm thickness were prepared from both whole rocks and euhedral quartz crystals from miarolitic cavities. The latter were preferentially cut parallel to the c-axis of the crystal. Basic investigation of the samples was performed by optical microscopy using reflected and transmitted light, and appropriate fluid, melt, and solid inclusions were selected based on petrographic time relationships, inclusion size, and state of preservation. Because one of the main goals of this study was to characterize the composition of magmatic bulk fluids, we focused our search on early, intermediate-density fluid inclusions rather than on later vapor and brine inclusions. Selected fluid, melt, and solid inclusions were analyzed by the following methods.

Microthermometry

Microthermometry was performed on a Linkam THSMG 600 heating-cooling stage that was calibrated to an uncertainty of ±0.1°C at –56.6°C and 0.0°C and to ±1°C at 374°C. Fluid salinity and homogenization temperature were determined for each inclusion, unless this was not possible due to small size. Most fluid inclusions contained enough CO_2 to form clathrates, but not enough to saturate in CO_2 liquid, in which case the accurate determination of fluid salinities is difficult. For these fluid inclusions, we used the software ICE (Bakker, 1997) to calculate salinities based on the melting points of ice and clathrate, the volume fraction of liquid, and Peng and Robinson's (1976) equation of state for the system (H_2O)-CO_2-CH_4-N_2-C_2H_6. This approach resulted in NaCl equiv values that were almost 50% lower than those calculated from ice melting temperatures and suggests CO_2 concentrations ranging from 2.0 to 7.9 mol % CO_2. In fluid inclusions that did not form clathrates upon freezing, NaCl equiv salinities were determined based on ice melting temperatures using the equations in Bodnar and Vityk (1994). Fluid isochores were constructed based on homogenization temperatures and recalculated NaCl equiv values using the formulas in Bodnar and Vityk (1994) and neglecting any influence of CO_2, as the study of Schmidt and Bodnar (2000) showed that addition of 4 mol % CO_2 to an aqueous fluid with a density of ~0.7 g/cm^3 ($Th_{tot\ (\rightarrow L)}$ ~350°C) and a salinity of 6 wt % NaCl results in only a small shift of the corresponding isochore.

Raman spectroscopy

Raman spectra were taken of solid inclusions as well as of the liquid and gaseous portions of fluid inclusions with a Horiba LabRAM HR 800 spectrometer connected to a Coherent Innova 90C argon ion laser situated at the Bayerisches Geoinstitut, using an exposure time of 20 s and two accumulations. The resulting spectra obtained from fluid inclusions were checked for the presence of H_2O, H_2S, SO_2, HSO_4^-, and CO_2 bands (Burke, 2001) without quantifying absolute abundances. Spectra of solid inclusions and mineral phases were compared with spectra currently available from databases such as the RRUFF Project (http://rruff.geo.arizona.edu/) and the online service from the Geofluids Laboratory at the University of Siena (http://www.dst.unisi.it/geofluids-lab/default.html).

Laser ablation-inductively coupled plasma-mass spectrometry

Laser ablation-inductively coupled plasma-mass spectrometry (LA-ICP-MS) measurements were performed at the Bayerisches Geoinstitut with a 193-nm ArF Excimer laser (Geolas M system; Coherent; USA) attached to a quadrupole mass spectrometer (Elan DRC-e; Perkin Elmer; Canada). The sample chamber was flushed with He gas at a rate of 0.4 l/min, to which 5 ml/min H_2 gas was added on the way to the ICP-MS (Guillong and Heinrich, 2007). Elements were measured on isotopes ^{7}Li, ^{11}B, ^{23}Na, ^{25}Mg, ^{27}Al, ^{32}S, ^{35}Cl, ^{39}K, ^{42}Ca, ^{49}Ti, ^{55}Mn, ^{57}Fe, ^{65}Cu, ^{66}Zn, ^{75}As, ^{85}Rb, ^{88}Sr, ^{89}Y, ^{90}Zr, ^{93}Nb, ^{98}Mo, ^{107}Ag, ^{118}Sn, ^{133}Cs, ^{140}Ce, ^{181}Ta, ^{184}W, ^{208}Pb, ^{209}Bi, ^{232}Th, and ^{238}U, using dwell times of 10 to 50 ms per isotope. The ICP-MS system was tuned to a thorium oxide rate of ~0.05% and a rate of doubly charged calcium ions of ~0.1%, according to measurements on NIST SRM 610 glass. External standardization was based on the afghanite standard described in Seo et al. (2011) for Cl and S, and on NIST SRM 610 glass using the values given in Spandler et al. (2011) for all other elements. Element concentration ratios measured in fluid and melt inclusions were then turned into absolute values by using the concentration of either Na or Al as internal standard. For fluid inclusions, we used Na from the microthermometrically determined (or determined via ICE program) NaCl equiv value and applied the empirical correction formula of Heinrich et al. (2003) to account for the effect of other major cations. For melt inclusions, we used the Al content of whole rocks from the same magma system that show similar degrees of melt fractionation (based on major and trace element ratios) as the melt inclusions (e.g., Halter et al., 2004a; Pettke, 2006). Detection limits depend on the size of the analyzed inclusion, and thus vary from analysis to analysis. For typical melt inclusions measuring 30 to 50 μm in diameter, the detection limit was <1 ppm for Rb, Sr, Y, Zr, Nb, Mo, Ag, Cs, Ce, Ta, W, Bi, Th, and U, 1 to 10 ppm for Li, B, Na, Mg, Cu, Zn, As, Sn, Ba, and Pb, 10 to 100 ppm for Ti, Mn, and Fe, 200 to 400 ppm for K, and 1 to 2 wt % for Ca. For intermediate-density fluid inclusions of similar size and a salinity of 5 to 10 wt % NaCl equiv, the detection limit was 1 to 10 ppm for Rb, Mo, Ag, Cs, Ce, W, and Bi, 10 to 100 ppm for B, Mn, Cu, Zn, As, Sn, and Pb, 100 to 1,000 ppm for Al and Fe, 0.1 to 1.0 wt % for S and K, several wt % for Cl, and 5 to 20 wt % for Ca. Combined analytical uncertainties are estimated at 10 to 20% (Heinrich et al., 2003; Halter et al., 2004a; Pettke, 2006), except for elements close to the detection limit. The concentrations of Li, Ti, and Al were corrected for the contribution of coablated host, which effect was significant in the case of Li and Ti, but insignificant in the case of Al.

Reequilibration experiments

One fluid inclusion trail of Drammen sample Dra 6B was first characterized by microthermometry, Raman spectroscopy, and LA-ICP-MS, and then cut out of the quartz wafer. The resulting quartz column was loaded together with

fluid and buffer minerals (muscovite, orthoclase, albite, and topaz to produce an acidic pH; plus chalcopyrite to buffer the Cu content) into a quartz capsule, which was itself welded into a gold capsule (Lerchbaumer and Audétat, 2012a). A small piece of etched quartz from Brazil was added, as well, to trap the loaded fluid, which had a major element composition similar to that of the already existing fluid inclusions in the quartz column. The experiment was run at 650°C and 140 MPa for 22 days. After cooling, the capsule was opened and the pH of the quench fluid was measured with indicator paper. Subsequently, both the reequilibrated Drammen sample and the small quartz piece containing newly formed fluid inclusions were polished and prepared for analysis. In the reequilibrated Drammen sample, only fluid inclusions <60 μm in size and from <~50-μm depth below the surface were analyzed. The results were then compared with the results obtained from fluid inclusions analyzed before reequilibration. Similar reequilibration experiments on both natural and synthetic fluid inclusions are described in Lerchbaumer and Audétat (2012b).

Results

An overview of the information obtained from melt and fluid inclusions, including fluid salinity, sulfur content, concentrations of Mo, Cu, and Cs, and estimated formation conditions is given in Table 1. The full data set is presented in Tables 2, 3, and 4.

Treasure Mountain dome

A total of 25 melt inclusions were analyzed from quartz phenocrysts in the leucocratic border phase (sample TM 7), from quartz grains in the granular facies (sample TM 2), and from quartz crystals in miarolitic cavities in the border phase (samples TM 10, TM 12) (Table 2). Because all these samples cooled slowly, the melt inclusions are now coarsely crystallized and consist of a cluster of several solid phases (e.g., feldspar, mica, oxides) surrounded by residual fluid (e.g., Roedder, 1984; Bodnar and Student, 2006; Audétat and Lowenstern, 2012; see Fig. 4C). Only inclusions that were fully surrounded by quartz and were not intersected by cracks or fluid inclusion trails were chosen for analysis. No attempt was made to rehomogenize the inclusions prior to analysis because they were ablated as a whole and, thus, their bulk composition was obtained by integrating the signal and subtracting the amount of ablated host (e.g., Halter et al., 2004a; Pettke, 2006). As internal standard for the calculation of absolute element values from LA-ICP-MS element ratios, we took the average Al concentration (12.8 wt % Al_2O_3) of whole-rock analyses of the leucocratic border phase reported in Mutschler et al. (1976). The good reproducibility of most elements in melt inclusion assemblages (e.g., in sample TM12A; see Bodnar and Student, 2006, for the definition of melt inclusion assemblages) demonstrates that they formed by homogeneous entrapment of a single phase. All melt inclusions are rhyolitic in composition (Table 2). With increasing degree of crystallization and fractionation, the residual melt becomes increasingly enriched in incompatible elements like Cs, Rb, W, and Mo, but depleted in compatible elements like Mg, Fe, Ti, Ca, and Sr. Plots of the concentrations of Ti, Mo, W, and Rb against Cs (which is the element that behaved most incompatibly) are shown in Figure 3. Titanium concentrations decrease regularly from melt inclusions analyzed in the leucocratic border phase over those analyzed in the granular facies to those analyzed in miarolitic quartz, whereas the concentrations of Rb, Mo, and W follow the opposite trend. In a closed system the observed increase from ~5 to ~90 ppm Cs in the residual melt requires a degree of crystallization of at least 90%. Thus, the melt inclusions analyzed in miarolitic quartz represent the very last melt fractions in an almost completely crystallized granite. The fact that the melt inclusions analyzed in the leucocratic border phase are less fractionated than those analyzed in the granular facies is somewhat unexpected because the higher SiO_2 content (Mutschler, 1976) and leucocratic appearance of the former rock suggests a higher degree of fractionation. However, the melt inclusions analyzed in the granular zone were hosted by relatively small quartz grains that may have crystallized after magma intrusion, for which reason they may be younger and thus more evolved than the ones analyzed in the phenocrysts in the leucocratic border phase. Either way, the analyses provide important insight into the behavior of ore metals and other trace elements during the crystallization of this granite. Molybdenum concentrations in the residual silicate melt increased from ~5 ppm at ~5 ppm Cs to ~35 ppm at ~90 ppm Cs, and W concentrations increased from ~2 to 20 ppm within the same crystallization interval, implying that both Mo and W behaved strongly incompatibly. Interestingly, the quartz phenocrysts in the border phase contain inclusions of molybdenite that were trapped at approximately the same time as the analyzed melt inclusions (Audétat et al., 2011), whereas no molybdenite inclusions were found in the three thick sections prepared from the granular facies. Together with the incompatible behavior of Mo noted above, this suggests that the intruding magma originally was molybdenite saturated, but then became molybdenite undersaturated at higher degrees of crystallization. The latter may have been caused by increasing f_{O_2} and/or decreasing f_{S_2} (Audétat et al., 2011). The Mo content (3 ppm), Zr content (126 ppm), and major element composition of a melt inclusion trapped next to a molybdenite inclusion in a quartz phenocryst of the border phase (TM 7C, MI 4) allow estimation of the conditions of melt entrapment. Zircon saturation thermometry (Watson and Harrison, 1983) returns a temperature of 780°C, whereas molybdenite saturation constrains log f_{O_2} at –15.1 (corresponding to the quartz-fayalite-magnetite buffer) and log f_{S_2} at –4.1 (corresponding to the pyrrhotite-quartz-fayalite invariant point), if it is assumed that the melt was additionally saturated in pyrrhotite (Audétat et al., 2011).

A cross section through a euhedral quartz crystal from miarolitic cavity TM 12 is shown in Figure 4. The crystal contains melt inclusions and intermediate-density (0.6–0.7 g/cm^3) fluid inclusions in its basal zone, vapor and brine inclusions (late-trapped brines approaching the composition of salt melts) in pseudosecondary trails in the next, comparatively clear growth zone, abundant solid inclusions of K-feldspar, muscovite, albite, fluorite, anhydrite, and pyrite in the overlying dark growth zone, and high-density aqueous inclusions (±very low density vapor inclusions) and solid inclusions of epidote, rutile, and chlorite in later growth zones. The intermediate-density fluid inclusions in the base of the crystal have

TABLE 1. Overview of Measured Samples from the Treasure Mountain Dome and the Drammen and Glitrevann Granites

Sample no.	Type of inclusion	n	Salinity (wt % NaCl equiv)	Th_{tot}[1] (°C)	to[1]	CO_2[2] (mol %)	Temperature (°C)[3]	Pressure (MPa)[3]	S (wt %)	Cs (ppm)	Mo (ppm)	Cu (ppm)	Mo/Cu
TM 5A	Fluid	5	6.2 ± 2.1	500	V	2.5–5.2	n.k.	n.k.	<0.35–0.52	87–160	1–3	12–100	0.026 ± 0.023
TM 5B	Fluid	6	4.4 ± 1.9	n.a.	V	3.2–5.7	n.k.	n.k.	<0.13–1.28	45–160	1–2	2–120	0.028 ± 0.029
TM 10A	Fluid	5	6.3 ± 1.6	430–530	V	2.6–7.9	n.k.	n.k.	0.49–0.61	26–73	5–7	<20–120	0.069 ± 0.048
TM 12A	Fluid	6	5.0 ± 1.3	n.a.	n.a.	3.3–6.0	n.k.	≤100[5]	n.a.	60–170	47–160	33–1,900	0.13 ± 0.18
TM 7 border phase	Melt	4	-	-	-	-	-	-	-	4–6	3–7	<2–11	0.68 ± 0.35
TM 2 granular facies	Melt	8	-	-	-	-	-	-	-	2–67	4–17	1–15	1.59 ± 1.48
TM 10A + 12A miar. Qtz	Melt	13	-	-	-	-	-	-	-	29–130	21–43	3–30	2.11 ± 1.90
Dra 2[6]	Melt	14	-	-	-	-	-	-	-	10–1,100	6–32	<1	>16.27
Dra 2B	Fluid	6	9.5 ± 0.5	n.a.	n.a.	<1.6[4]	n.k.	n.k.	0.52	520–970	4–65	8–3,500	0.022 ± 0.044
Dra 6A	Fluid	3	5.8	425	L	2.2–2.4	650–700	130–150	<0.67	58–280	26–48	410–1,500	0.044 ± 0.040
Dra 6A	Melt	3	-	-	-	-	-	-	-	92–100	14–18	<2	>8.00
Dra 6B	Fluid	5	5.7 ± 0.2	420	L	2.3	650–700	130–150	0.20–0.30	180–250	20–46	530–2,600	0.019 ± 0.012
Dra 6B	Melt	3	-	-	-	-	-	-	-	93–190	21–26	<3	>7.67
Dra 20	Fluid	2	11.0 ± 1.5	~550	M	<1.6[4]	n.k.	n.k.	<1.09	240–360	150–270	58–90	2.79 ± 1.47
Glt 2B	Fluid	4	6.7 ± 0.7	~520	V	2.7–3.3	n.k.	n.k.	0.66	22–76	<3–5	17–180	0.085 ± 0.113
Glt 3A	Fluid	6	8.1 ± 2.6	n.a.	n.a.	2.0–3.5	n.k.	n.k.	<0.19–0.53	35–130	<1–8	5–17	0.40 ± 0.43
Glt granite	Melt	4	-	-	-	-	-	-	-	20–65	11–13	<4	>2.95

- = not applicable; miar. Qtz = miarolitic quartz; n = number of analyses; n.a. = not analyzed; n.k. = not known because fluid inclusions are not clearly cogenetic with melt inclusions

[1] Homogenization temperature to liquid (L) or vapor (V) or by fading of the mensicus (M)

[2] Calculated from clathrate melting point using the software ICE (Bakker, 1997)

[3] Estimated conditions of inclusion formation

[4] Minimum concentration of CO_2 necessary to form clathrates (in the simple H_2O-CO_2 system; Hedenquist and Henley, 1985)

[5] Based on the presence of solid inclusions of andalusite

[6] Section through aplitic granite, pegmatitic zone, and miarolitic quartz

TABLE 2. LA-ICP-MS Data of Melt Inclusions

Sample no.	$Na_2O_{meas.}$[1] (wt %)	$Na_2O_{est.}$[1] (wt %)	MgO (wt %)	Al_2O_3[2] (wt %)	K_2O (wt %)	$CaO_{meas.}$[3] (wt %)	$CaO_{est.}$[3] (wt %)	TiO_2 (wt %)	MnO (wt %)	FeO_{tot} (wt %)	SiO_2[4] (wt %)	Cu (ppm)	Zn (ppm)	As (ppm)
Treasure Mt #229[5]	3.83	-	0.09	12.89	4.53	0.39	-	0.11	0.07	0.69	77.4	n.a.	n.a.	n.a.
Treasure Mt #300[5]	3.13	-	0.08	12.81	5.04	0.29	-	0.11	0.00	0.55	77.9	n.a.	n.a.	n.a.
Treasure Mountain granite, leucocratic border zone														
TM 7B, MI 3	0.50	3.50	0.04	12.8	3.5	0.41	-	0.15	0.06	0.40	78.8	6	116	n.a.
TM 7A, MI 1	0.32	3.50	0.02	12.8	3.5	0.35	-	0.08	0.06	0.34	79.2	12	56	n.a.
TM 7C, MI 4	0.30	3.50	0.03	12.8	3.5	0.49	-	0.04	0.07	0.47	78.9	<2	58	n.a.
TM 7E, MI 5	0.30	3.50	0.03	12.8	3.5	0.44	-	0.11	0.06	0.41	78.9	7	46	n.a.
Treasure Mountain, granular zone														
TM 2, MI 2	0.30	3.50	0.03	12.8	3.9	<1.2	0.30	0.07	0.05	0.42	78.8	12	31	2
TM 2, MI 7	0.31	3.50	0.02	12.8	3.5	<3.0	0.30	0.07	0.07	0.37	79.2	<7	25	2
TM 2, MI 8	5.05	3.50	0.02	12.8	3.0	<0.7	0.30	0.05	0.06	0.31	79.8	1	33	4
TM 2, MI 1	0.35	3.50	0.02	12.8	3.6	<3.0	0.30	0.06	0.09	0.30	79.2	2	30	4
TM 2, MI 5	0.37	3.50	0.02	12.8	3.4	<1.0	0.30	0.04	0.08	0.36	79.3	<2	40	5
TM 2, MI 4	0.36	3.50	0.02	12.8	3.5	<9.6	0.30	0.05	0.09	0.26	79.3	<20	32	5
TM 2, MI 3	0.28	3.50	0.00	12.8	3.3	<3.8	0.30	0.01	0.07	0.11	79.8	6	21	9
TM 2, MI 9	0.30	3.50	0.02	12.8	3.4	<5.4	0.30	0.05	0.09	0.24	79.5	16	25	3
Treasure mountain, miarolitic quartz														
TM 10A1, MI 5	0.13	3.50	0.02	12.8	2.4	<5.4	0.20	0.04	0.15	0.34	80.3	4	87	2
TM 10A2, MI 2	0.30	3.50	n.a.	12.8	3.6	<6.3	0.20	n.a.	0.09	0.35	79.2	<6	31	7
TM 10A1, MI 2	0.23	3.50	0.02	12.8	2.8	<2.4	0.20	0.04	0.10	0.36	80.0	<4	38	7
TM 10A1, MI 7	0.39	3.50	0.02	12.8	3.1	<17.5	0.20	<0.01	0.09	0.25	79.9	<37	44	<21
TM 10A1, MI e1	0.34	3.50	0.02	12.8	2.9	0.25	-	0.04	0.09	0.33	79.9	<5	33	9
TM 10A1, MI 1	0.27	3.50	0.02	12.8	2.6	<4.2	0.20	0.03	0.09	0.32	80.3	23	33	8
TM 10A2, MI 1	0.38	3.50	n.a.	12.8	3.4	<3.2	0.20	n.a.	0.08	0.30	79.5	<4	32	6
TM 10A1, MI 3	0.36	3.50	n.a.	12.8	3.8	<7.6	0.20	n.a.	0.08	0.29	79.1	<10	32	8
TM 12A1, MI 1	0.29	3.50	n.a.	12.8	3.8	n.a.	0.20	n.a.	0.10	0.20	79.2	<18	19	11
TM 12A1, MI 2	0.30	3.50	n.a.	12.8	3.9	n.a.	0.20	n.a.	0.10	0.13	79.2	31	<53	10
TM 12A1, MI 3	0.24	3.50	0.01	12.8	3.1	<1.9	0.20	0.03	0.12	0.28	79.8	4	50	8
TM 12A1, MI 4	0.21	3.50	0.01	12.8	2.8	<2.5	0.20	0.04	0.11	0.29	80.1	<5	31	7
TM 12A1, MI 5	0.23	3.50	0.01	12.8	3.0	<1.7	0.20	0.03	0.11	0.27	80.0	<4	35	10
Drammen 14[6]	3.95	-	n.a.	12.64	4.22	0.29	-	0.09	0.09	0.50	78.0	n.a.	n.a.	n.a.
Drammen 60[6]	3.58	-	0.06	12.35	4.39	0.36	-	0.11	0.11	0.63	78.1	n.a.	n.a.	n.a.
Dra 6A, MI 1	0.23	3.80	0.01	12.5	2.7	<0.9	0.20	0.03	0.08	0.36	80.2	<2	29	25
Dra 6B, MI e1	0.27	3.80	0.01	12.5	3.9	0.07	-	0.03	0.07	0.31	79.3	<3	25	46
Dra 6B, MI 4	0.20	3.80	0.02	12.5	3.5	<3.8	0.20	0.03	0.10	0.37	79.4	<8	26	30
Dra 6A, MI 2	0.27	3.80	0.02	12.5	3.2	<2.0	0.20	0.03	0.09	0.44	79.6	<4	36	29
Dra 6A, MI 4	0.25	3.80	<0.04	12.5	3.3	<22.7	0.20	0.03	0.09	0.30	79.7	<39	46	22
Dra 6B, MI 3	0.22	3.80	0.00	12.5	3.9	<3.7	0.20	0.02	0.02	0.09	79.5	<8	8	42
Section through Drammen granite, pegmatitic zone and miarolitic quartz														
Dra 2 MI 1 granite	0.29	3.80	0.03	12.5	3.8	<1.5	0.30	0.03	0.07	0.48	78.9	<2	26	6
Dra 2 MI 2 granite	0.28	3.80	0.02	12.5	3.6	<4.8	0.30	0.04	0.07	0.47	79.1	<10	30	<5
Dra 2 MI 3 granite	0.27	3.80	0.02	12.5	3.2	<1.3	0.20	0.04	0.08	0.34	79.7	<3	28	7
Dra 2 MI 4 granite	0.37	3.80	0.02	12.5	3.6	<1.8	0.20	0.03	0.08	0.48	79.2	<4	41	20
Dra 2 MI 5 granite	0.39	3.80	0.02	12.5	3.7	<1.5	0.20	0.04	0.09	0.42	79.1	<3	34	34
Dra 2 MI 6 granite	0.26	3.80	0.01	12.5	3.4	<1.7	0.20	0.02	0.08	0.14	79.8	<4	22	60
Dra 2 MI 1, pegm. z.	0.38	3.80	0.01	12.5	3.4	<2.6	0.20	0.03	0.08	0.35	79.5	<5	30	23
Dra 2 MI 2, pegm. z.	0.35	3.80	0.01	12.5	3.4	<1.1	0.20	0.02	0.09	0.28	79.6	<2	28	35
Dra 2B, MI 2, Qtz	0.11	3.80	0.01	12.5	2.9	<2.0	0.10	0.02	0.07	0.18	80.4	<4	19	55
Dra 2B, MI 3, Qtz	0.17	3.80	0.01	12.5	3.2	<2.7	0.10	0.02	0.07	0.18	80.0	<5	19	47
Dra 2B, MI 1, Qtz	0.26	3.80	0.01	12.5	2.9	<5.8	0.10	0.02	0.07	0.12	80.4	<10	11	60
Dra 2 MI 1, Qtz	0.22	3.80	0.01	12.5	2.9	<4.4	0.10	0.02	0.07	0.14	80.5	<10	13	62
Dra 2 MI 2, Qtz	0.22	3.80	0.01	12.5	3.1	<5.7	0.10	0.02	0.07	0.16	80.2	<12	15	65
Dra 2 MI 3, Qtz	0.17	3.80	0.01	12.5	3.1	<0.8	0.10	0.02	0.08	0.16	80.2	0.1	13	72
Glitrevann 3[7]	4.50	-	n.a.	12.30	4.69	0.29	-	0.15	0.05	0.86	76.8	n.a.	n.a.	n.a.
Glitrevann 5[7]	4.40	-	n.a.	12.10	4.53	0.36	-	0.10	0.02	0.79	77.4	n.a.	n.a.	n.a.
Glt 2, MI 2	4.88	4.88	0.04	12.2	3.4	<8.1	0.20	0.07	0.06	0.58	78.3	<19	97	42
Glt 2, MI 3	0.34	4.60	0.03	12.2	3.3	<2.2	0.20	0.08	0.05	0.49	78.9	<5	35	10
Glt 3, MI 3	0.23	4.60	0.04	12.2	3.4	<3.4	0.20	0.07	0.05	0.48	78.7	<4	33	16
Glt 3, MI 9	0.30	4.60	0.02	12.2	3.3	<6.9	0.20	0.05	0.05	0.42	79.0	<14	36	39

- = not applicable; n.a. = not analyzed

[1] Measured Na_2O values ($Na_2O_{meas.}$) are low due to postentrapment loss of Na (Zajacz et al., 2008); original Na_2O concentrations ($Na_2O_{est.}$) are estimated from listed whole-rock data

[2] Al_2O_3 values used for internal standardization are average concentrations from listed whole-rock data

[3] CaO concentrations below detection limit are estimated from whole-rock data

[4] SiO_2 values are estimated by subtracting the sum of all other major element oxides from 100 wt %

with Reference Data of Whole-Rock Analyses

Li (ppm)	B (ppm)	Rb (ppm)	Sr (ppm)	Y (ppm)	Zr (ppm)	Nb (ppm)	Mo (ppm)	Ag (ppm)	Sn (ppm)	Cs (ppm)	Ba (ppm)	Ce (ppm)	Ta (ppm)	W (ppm)	Pb (ppm)	Bi (ppm)	Th (ppm)	U (ppm)
n.a.	n.a.	n.a.	n.a.	n.a.	n.a.	n.a.	n.a.	n.a.	n.a.	n.a.	n.a.	n.a.	n.a.	n.a.	n.a.	n.a.	n.a.	n.a.
n.a.	n.a.	n.a.	n.a.	n.a.	n.a.	n.a.	n.a.	n.a.	n.a.	n.a.	n.a.	n.a.	n.a.	n.a.	n.a.	n.a.	n.a.	n.a.
n.a.	n.a.	400	12	22	120	39	5	n.a.	<10	4	5	59	3	<2	25	n.a.	29	7
n.a.	n.a.	440	0.7	33	82	58	7	n.a.	<12	5	4	65	3	<3	23	n.a.	37	10
n.a.	n.a.	450	0.5	126	130	120	3	n.a.	11	6	<2	49	5	3	25	n.a.	49	20
n.a.	n.a.	340	1.4	28	100	44	7	n.a.	<6	7	3	70	3	<3	27	n.a.	36	9
49	15	470	5.3	24	110	67	9	1.0	5	2	14	76	5	5	28	0.6	66	22
62	22	660	2.2	32	95	120	13	<0.7	<21	17	3	53	6	5	15	<0.4	33	17
<1	24	460	3.8	25	88	110	10	<0.3	5	18	15	56	8	7	28	0.8	44	25
56	25	760	2.1	42	68	130	4	<0.7	6	19	6	29	8	7	18	1.3	40	34
39	28	740	1.6	30	79	130	15	<0.3	9	31	2	52	8	7	31	1.1	37	29
<18	25	940	3.5	36	89	150	16	<2.9	<57	51	<6	48	11	7	25	1.0	35	37
26	71	1,200	3.2	3	76	21	18	<1.3	<25	57	<4	11	2	8	21	1.6	18	12
24	32	870	3.7	28	75	90	10	<1.4	<40	71	24	59	7	5	16	<1.2	42	22
65	17	830	0.3	47	85	150	22	<1.6	<37	31	<8	65	18	25	24	0.8	30	30
n.a.	46	880	n.a.	n.a.	n.a.	n.a.	34	<2.1	<40	56	n.a.	73	n.a.	30	29	1.1	n.a.	n.a.
84	47	810	0.2	45	55	150	32	<0.6	9	67	<3	47	24	27	28	1.2	20	27
<43	<81	1,200	<3.1	41	65	130	26	<6.2	<100	70	<21	68	13	21	26	<2.5	25	25
59	49	890	<0.5	40	81	150	36	<1.4	9	79	<3	69	22	28	29	1.2	30	31
69	55	860	<1.3	39	73	140	31	<1.1	<23	80	<5	82	21	26	28	1.5	33	26
n.a.	41	1,000	n.a.	n.a.	n.a.	n.a.	32	<0.8	<25	81	n.a.	68	n.a.	28	25	1.1	n.a.	n.a.
n.a.	43	1,500	n.a.	n.a.	n.a.	n.a.	35	<1.7	<56	95	n.a.	63	n.a.	25	31	1.6	n.a.	n.a.
n.a.	58	1,300	n.a.	n.a.	n.a.	n.a.	33	n.a.	<85	83	n.a.	89	n.a.	19	25	1.4	n.a.	n.a.
n.a.	53	1,200	n.a.	n.a.	n.a.	n.a.	39	n.a.	<71	95	n.a.	21	n.a.	16	23	<1.4	n.a.	n.a.
35	50	1,000	0.5	29	82	120	33	<0.9	10	100	<3	90	19	18	30	2.2	27	22
27	44	900	<0.5	33	91	130	27	<1.0	9	100	<3	73	13	16	21	1.1	37	30
38	57	1,000	<0.5	27	86	130	45	<0.4	11	140	<2	69	15	22	28	1.9	26	26
14	n.a.	430	26	18	139	n.a.	6	n.a.	4	n.a.	n.a.	n.a.	n.a.	10	n.a.	n.a.	n.a.	n.a.
2	n.a.	330	32	12	110	n.a.	27	n.a.	4	n.a.	n.a.	n.a.	n.a.	1	n.a.	n.a.	n.a.	n.a.
130	120	950	0.1	22	92	180	14	<0.3	9	92	<1	51	26	16	20	2.2	21	15
530	190	970	0.1	3	80	190	26	<0.5	12	190	<2	31	35	23	21	4.0	19	15
660	130	990	0.3	20	71	190	21	<2.0	14	93	<5	53	33	17	15	1.3	21	12
360	140	1,100	0.2	38	250	200	17	<0.8	13	100	<2	46	17	16	22	2.5	43	33
230	120	1,200	<5.0	35	220	180	18	<5.8	<150	100	<19	48	17	11	21	<7.1	34	25
500	200	1,400	0.5	9	70	190	24	<1.4	9	160	<3	44	35	23	20	4.5	22	16
140	16	730	0.8	14	95	110	11	0.1	8	10	2	62	7	9	24	1.5	43	29
130	<22	810	0.3	0	140	120	14	<1.3	<21	10	<4	21	9	9	8	<0.8	58	33
110	39	890	0.7	17	100	100	12	<0.4	8	31	1	61	8	9	13	1.5	43	26
160	110	820	0.3	18	120	110	14	<0.5	9	53	<2	57	5	9	8	1.5	46	30
190	170	1,100	0.2	38	140	250	31	<0.6	14	73	<2	66	26	27	20	2.8	45	13
66	320	1,200	0.9	10	28	92	32	<0.5	10	240	1	33	74	31	12	7.6	12	14
140	140	960	<0.4	30	140	170	17	<1.0	12	97	<2	62	16	15	25	2.4	44	36
120	160	1,200	0.2	27	120	200	19	<0.4	14	130	<1	67	18	18	21	3.0	35	29
390	180	1,400	0.2	14	57	96	29	<0.8	13	270	<2	68	18	30	11	12	20	12
400	250	1,500	0.3	11	66	93	24	<0.7	12	340	<3	53	21	30	9	10	17	13
200	220	1,600	0.6	5	42	59	5	<2.0	<35	430	<7	29	16	44	11	3.8	18	20
170	210	1,400	<0.8	6	24	52	6	<1.8	<26	840	<4	29	17	38	11	3.5	10	16
300	270	1,500	<1.1	7	28	58	7	<1.6	<33	1,000	<4	34	20	43	12	3.9	13	19
370	260	1,600	<0.2	6	34	60	6	0.1	8	1,100	<1	32	22	44	14	4.4	13	22
n.a.	n.a.	200	23	n.a.	n.a.	150	n.a.	n.a.	n.a.	n.a.	44	n.a.	n.a.	n.a.	n.a.	n.a.	n.a.	n.a.
n.a.	n.a.	240	12	n.a.	n.a.	130	n.a.	n.a.	n.a.	n.a.	11	n.a.	n.a.	n.a.	n.a.	n.a.	n.a.	n.a.
33	160	260	2.3	16	110	70	11	<2.5	<44	39	4	65	4	6	22	0.8	35	10
12	52	420	0.8	12	120	76	11	<1.0	<19	20	<3	48	5	4	10	0.4	34	13
10	68	550	0.8	54	120	190	13	<0.7	8	45	2	54	14	7	13	0.5	53	31
21	220	550	0.9	29	15	130	12	<2.1	<41	65	2	27	20	10	13	0.7	10	13

[5] Mutschler et al., 1976
[6] Ihlen et al., 1982
[7] Jensen, 1985

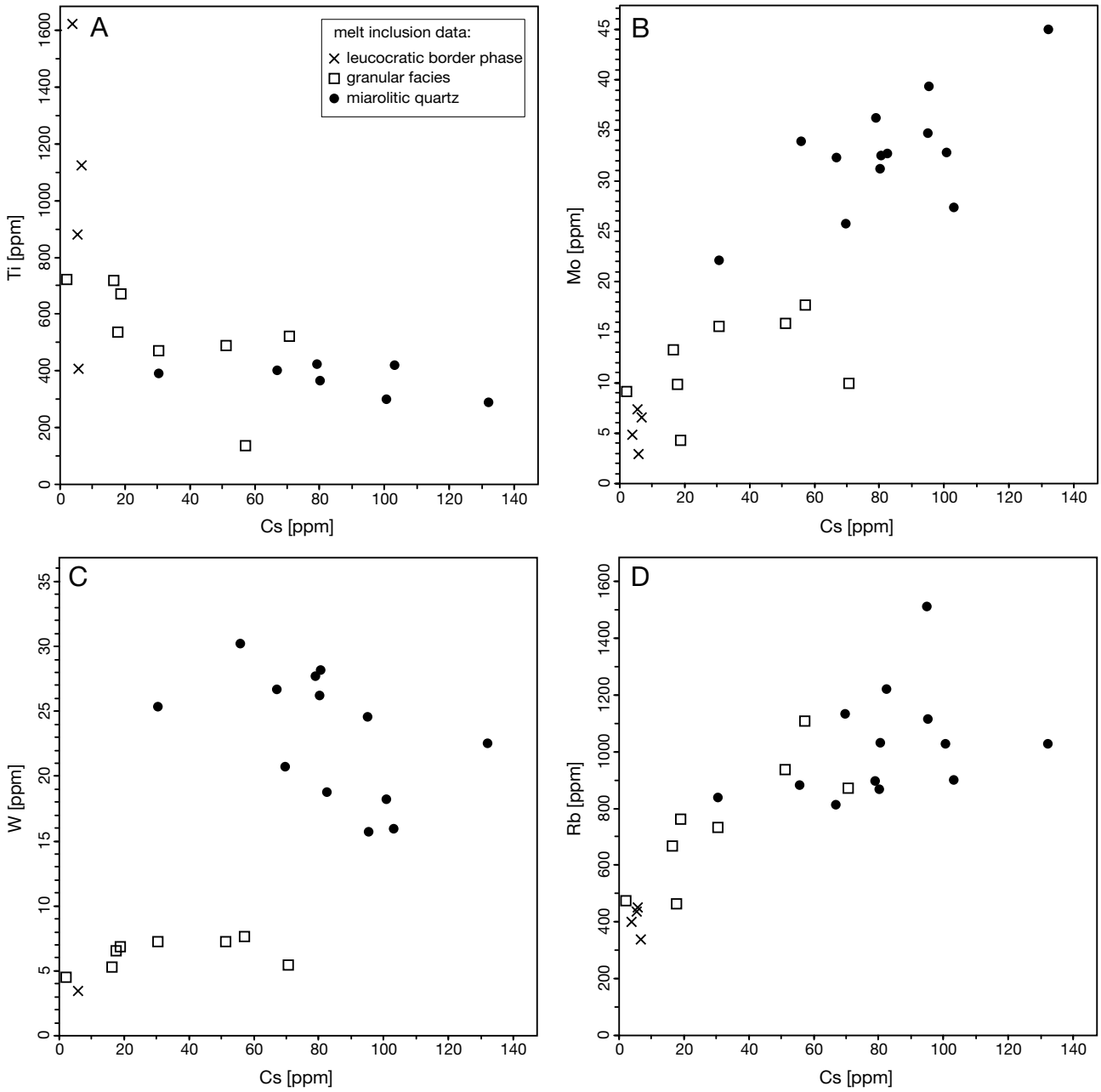

FIG. 3. (A-D) Compositional evolution of silicate melts in the Treasure Mountain dome, as recorded by quartz-hosted melt inclusions. Cesium is used in the abscissa because it is one of the most incompatible elements in granitic magmas and thus is an ideal indicator of melt fractionation.

salinities of 5 ± 1.3 wt % NaCl equiv. Homogenization temperatures were not determined for these inclusions because their number was very limited and we did not want to risk their decrepitation before they could be analyzed by LA-ICP-MS. Quartz crystals from miarolitic cavity TM 10 do not contain melt inclusions but, apart from that, record a very similar fluid evolution. The succession from intermediate-density fluid inclusions with salinities of 5 to 10 wt % NaCl equiv and relatively low homogenization temperatures (300°–550°C) over immiscible vapor and brine inclusions with increasingly disparate salinities and higher homogenization temperatures (>550°C) (with or without coexisting melt inclusions) to low-salinity aqueous fluid with densities ≥0.8 to 0.9 g/cm^3 is typical for quartz crystals from miarolitic cavity-bearing granites in general and reflects the evolution of originally single-phase, magmatic fluids as they enter the two-phase field upon decompression and cooling, and finally get diluted/superseded by invading meteoric water (e.g., Audétat and Pettke, 2003; Audétat et al., 2008). Since our main goal is to characterize the composition of the magmatic bulk fluid, only data from the intermediate-density fluid inclusions are presented here.

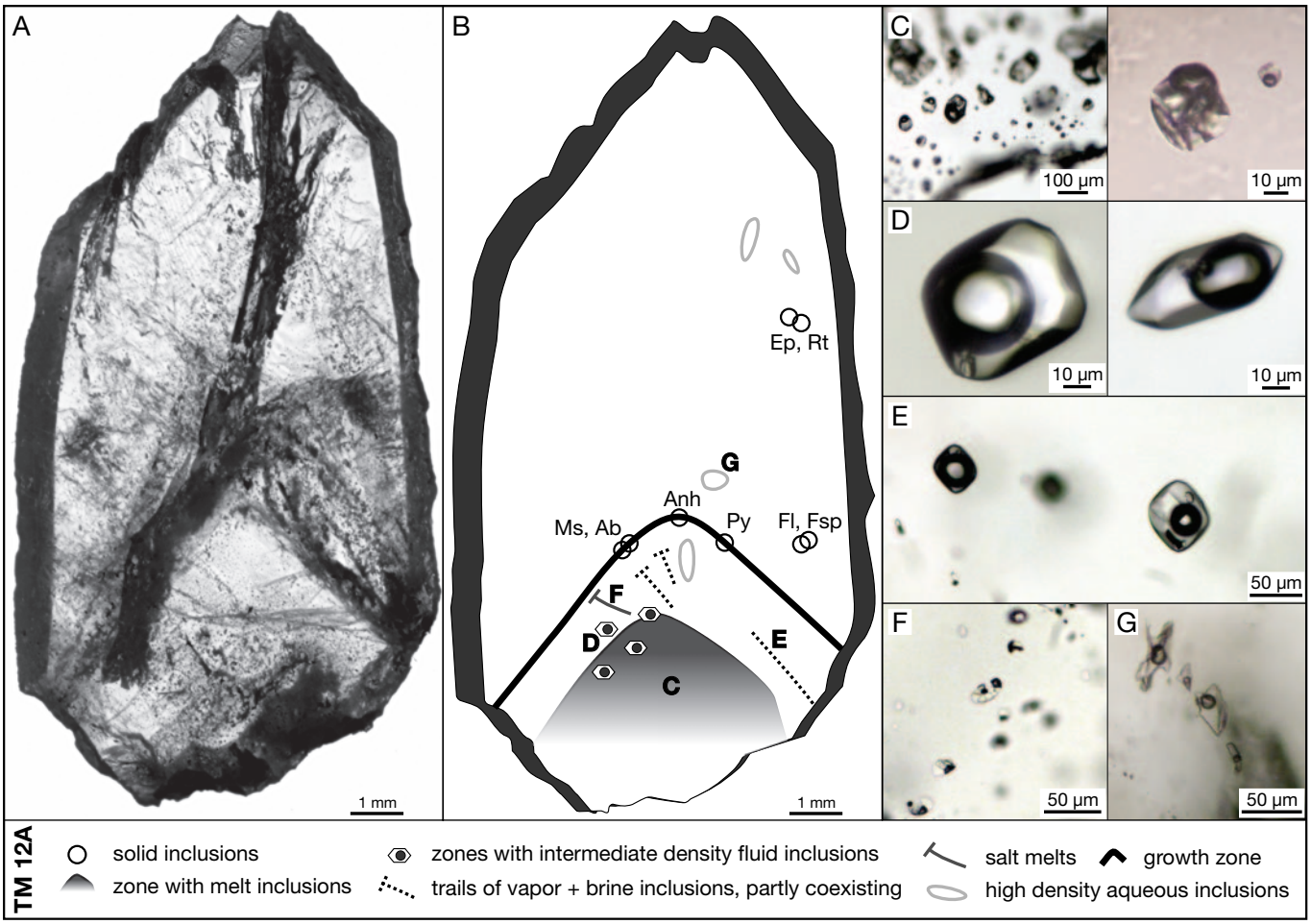

FIG. 4. (A) Photograph of a thick section through a quartz crystal from a miarolitic cavity in the Treasure Mountain dome (sample TM12A), cut parallel to the c-axis of the crystal. (B) Sketch of the same sample showing petrographic relationships between different types of melt, fluid, and solid inclusions (Ab = albite, Anh = anhydrite, Ep = epidote, Fl = fluorite, Fsp = feldspar [both plagioclase and K-feldspar], Ms = muscovite, Py = pyrite, Rt = rutile). (C-G) Photomicrographs of melt inclusions (C), early, intermediate-density fluid inclusions (D), coexisting vapor and brine inclusions (E), salt melts (F), and late, high-density aqueous inclusions (G), with their corresponding location indicated in the sketch map.

The compositions of 22 intermediate-density fluid inclusions analyzed in quartz from three different miarolitic cavities (TM 5, TM 10, TM 12) are listed in Table 3. Of those, only the inclusions from cavity TM 12 coexist with melt inclusions and thus are certain to represent magmatic fluids, whereas the inclusions analyzed from the other two samples may have formed at subsolidus conditions. Distinctly higher concentrations of Al in inclusions from the former sample (indicating a higher amount of dissolved silicates) support this interpretation.

Because we did not determine the homogenization temperatures of intermediate-density fluid inclusions in sample TM 12, we are unable to reconstruct entrapment conditions based on the intersection of fluid isochores with the granite solidus (e.g., Audétat and Pettke, 2003). However, an upper pressure limit of ~100 MPa (at 700°C) is indicated by the occurrence of andalusite in metamorphosed shales at the contact of the leucocratic border phase to the overlying sediments, whereas a value of 100 MPa was estimated for contact-metamorphosed limestone at the base of Treasure Mountain (Everett and Hoisch, 2008). Molybdenum concentrations are low (2–5 ppm) in the intermediate-density fluid inclusions analyzed from samples TM 5 and TM 10, but high (50–150 ppm) in the ones from sample TM 12, suggesting that most Mo precipitated from the magmatic-hydrothermal fluid at temperatures not far below the solidus. In contrast, the concentrations of most other elements remained constant within a factor of ~2 to 3. A notable exception is Cu, which varies by a factor of 6 to 60 in all three samples. CO_2 and S concentrations vary from 2.5 to 7.9 mol % and <0.13 to 1.3 wt %, respectively, with 80% of the latter values ranging between 0.3 and 0.7 wt %. Raman spectra reveal that S occurs mostly as SO_4^{-2} in the liquid portion of the fluid inclusions at ambient conditions. According to the experimental study of Zhang et al. (2012), molybdenum speciation in sulfur- and chlorine-bearing fluids is dominated by thiomolybdate complexes (most likely $NaHMoO_2S_2$). A molybdenite solubility of 50 to 150 ppm Mo in aqueous fluids containing 5 wt % dissolved NaCl would, for example, be reached at 650° to 700°C and f_{O_2}-f_{S_2} conditions close to the magnetite-pyrrhotite-pyrite

TABLE 3. LA-ICP-MS

Sample no.	Tm_{ICE} (–°C)	Tm_{CLATH} (°C)	$NaCl_{equiv.}$ [1] (wt %)	CO_2 [2] (mol %)	Na (wt %)	Al (wt %)	S (wt %)	Cl (wt %)	K (wt %)	Ca (wt %)	Mn (wt %)
Treasure mountain, miarolitic quartz											
TM 5A, FI 1b	10.0	4.1	8.2	5.2	2.5	0.14	0.4	5.6	0.9	<13	0.18
TM 5A, FI 4	5.0	–0.9	5.0	2.5	1.5	0.08	<0.6	4.6	0.4	<13	0.41
TM 5A, FI 3	6.5	5.6	5.1	5.1	1.6	0.25	0.4	3.1	0.5	<15	0.27
TM 5A, FI 7	5.3	6.0	4.0	5.0	1.2	<0.03	0.5	4.0	0.6	<19	0.19
TM 5A, FI 1a	10.3	3.4	8.8	4.9	2.5	0.06	<0.4	4.8	0.8	<9	0.78
TM 5B, FI 4	3.4	2.9	2.6	3.2	0.7	0.002	<0.1	1.7	0.3	<2	0.29
TM 5B, FI 5	4.1	n.v.	3.2	4.1	1.0	0.05	1.3	2.2	0.3	<8	0.13
TM 5B, FI 7	5.8	4.7	4.9	4.4	1.4	0.08	0.7	2.9	0.5	<10	0.30
TM 5B, FI 2b	3.7	3.5	2.9	3.4	0.9	0.06	0.3	2.5	0.3	<18	0.19
TM 5B, FI 1	6.4	n.v.	5.3	4.7	1.6	<0.02	0.4	4.8	0.7	<5	0.26
TM 5B, FI 2a	10.0	n.v.	7.6	5.7	1.9	0.08	0.2	5.6	1.0	<21	0.88
TM 10A1, trail B, FI 1	9.9	5.5	7.1	6.1	1.9	0.35	<2.6	9.3	0.9	<38	0.47
TM 10A1, trail B, FI 2	10.3	4.5	8.1	5.5	2.2	<0.10	<5.8	8.0	1.1	<97	0.49
TM 10A1, FI 2	7.8	8.0	4.9	7.9	1.4	<0.03	0.5	5.0	0.5	<15	0.35
TM 10A1, FI e1	n.v.	n.v.	7.1	5.2	2.0	0.16	0.6	4.0	1.5	<8	0.34
TM 10A2, FI 1	5.5	5.2	4.5	4.6	1.1	0.19	<1.7	<6.1	0.6	<35	0.33
TM 12A1, FI 3	4.4	3.0	3.8	3.4	0.4	5.3	n.a.	n.a.	2.3	n.a.	0.16
TM 12A1, FI 6	n.v.	n.v.	4.1	4.3	1.1	0.16	n.a.	n.a.	0.7	n.a.	0.19
TM 12A1, FI 1	8.1	0.5	8.3	3.3	2.0	0.53	n.a.	n.a.	1.5	n.a.	0.63
TM 12A1, FI 5	n.v.	5.0	4.1	4.3	0.8	2.1	n.a.	n.a.	1.6	n.a.	0.17
TM 12A1, FI 2b	4.5	n.v.	3.6	4.2	1.2	0.84	n.a.	n.a.	<0.7	n.a.	0.22
TM 12A2, FI 7	9.6	n.v.	7.0	6.0	1.8	1.2	n.a.	n.a.	1.5	n.a.	0.39
Drammen granite, miarolitic quartz											
Dra 2B, trail F, FI 1	6.4	-	9.7	<1.6[3]	3.2	<0.02	<0.9	8.2	0.8	<16	0.48
Dra 2B, trail F, FI 3	6.6	-	10.0	<1.6[3]	2.9	<0.03	0.5	7.0	1.3	<36	0.65
Dra 2B, trail F, FI 4	6.4	-	9.7	<1.6[3]	3.2	<0.03	<2.5	7.0	0.9	<35	0.42
Dra 2B, FI 1	5.7	-	8.8	<1.6[3]	2.7	0.51	<1.5	5.6	1.1	<22	0.36
Dra 2B, FI 2	6.3	-	9.6	<1.6[3]	3.2	0.24	<1.5	8.2	1.0	<26	0.25
Dra 2B, FI 4	5.8	-	9.0	<1.6[3]	3.0	<0.05	<2.6	7.0	<0.9	<42	0.16
Dra 6A, trail B, FI 2	5.5	–1.8	5.8	2.4	1.7	0.41	<2.0	7.6	1.0	<41	0.09
Dra 6A, trail B, FI 3	5.5	–1.8	5.8	2.4	1.8	0.20	<0.7	6.7	0.8	<14	0.18
Dra 6A, trail B, FI 5	5.5	–1.8	5.8	2.4	1.4	0.23	<1.3	7.1	1.5	<24	0.19
Dra 6B, FI 4	6.5	-	9.9	<1.6[3]	2.5	0.50	<2.8	13.8	2.3	<18	0.41
Dra 6B, trail A, FI 3	5.4	–1.8	5.6	2.4	1.9	0.49	<2.2	7.7	<0.6	<28	0.30
Dra 6B, trail A, FI 5	5.4	–1.8	5.7	2.4	1.5	0.19	<0.4	3.9	1.2	<7	0.24
Dra 6B, trail A, FI 6	5.4	–1.8	5.7	2.4	1.7	0.11	0.3	3.8	1.1	<3	0.07
Dra 6B, trail A, FI 7	5.4	–1.8	5.7	2.4	1.6	0.15	0.2	5.4	1.4	<7	0.07
Dra 20, FI 1	6.6	-	10.0	<1.6[3]	3.2	<0.02	<1.1	11.1	0.7	<16	0.38
Dra 20, FI 2	8.3	-	12.1	<1.6[3]	2.6	0.54	<1.7	10.4	1.6	<29	0.68
Glitrevann granite, miarolitic quartz											
Glt 2B, FI 5	6.3	1.5	6.2	3.3	1.8	<0.07	<1.9	5.2	0.8	<39	0.31
Glt 2B, FI 4	6.2	n.v.	6.1	3.2	2.0	<0.03	<0.7	6.2	0.6	<16	0.19
Glt 2B, FI 2	7.1	–1.0	7.5	2.7	2.0	0.07	0.7	4.7	0.9	<17	0.19
Glt 2B, FI 8	n.v.	n.v.	6.9	3.1	2.2	0.07	<1.4	7.0	0.7	<33	0.44
Glt 3A, FI 2	n.v.	n.v.	7.0	3.1	2.4	0.08	0.5	3.8	0.7	<5	0.10
Glt 3A, FI 4	5.5	2.4	5.1	3.5	1.2	0.03	<0.6	3.1	0.5	<11	0.44
Glt 3A, FI 14	n.v.	n.v.	7.0	3.1	2.3	0.03	<0.2	4.2	0.7	<5	0.13
Glt 3A, FI 6	7.6	0.9	7.6	3.3	2.6	0.11	<0.2	5.3	0.8	<6	0.11
Glt 3A, FI 1	9.6	0.5	9.6	3.5	3.2	0.03	<0.6	6.5	1.0	<14	0.45
Glt 3A, FI 3	10.5	–6.4	12.5	2.1	4.4	0.02	<0.2	8.1	1.2	<5	0.15

- = not applicable; n.a. = not analyzed; n.v. = not visible

[1]Salinity was corrected for clathrates using ICE software (Bakker, 1997); for inclusions, where no ice melting and/or clathrate melting could be observed, the average of the sample was used to calculate absolute LA-ICP-MS values; in the Drammen samples, clathrate melting occurred before ice melting; thus, no correction was necessary

triple point (Zhang et al., 2012), which appears reasonable considering the oxidized nature of sulfur in the fluid inclusions and the subsolidus evolution of f_{O_2} and f_{S_2} reconstructed for porphyry Mo deposits (Seedorff et al., 2005).

Fluid/melt partition coefficients calculated from the averages of five melt inclusions and six coexisting fluid inclusions in sample TM 12 are presented in Figure 5. Generally, the partition coefficients agree well with those determined on coexisting melt inclusions and low-salinity fluid inclusions from other granites, which, in turn, were shown to be compatible with experimental data (Zajacz et al., 2008). The highest values are observed for Pb, Zn and, potentially, Cu (notice the large uncertainty associated with the latter element), while Ce and Al display the least preference for the fluid phase. At the

Data of Fluid Inclusions

Fe (wt %)	B (ppm)	Cu (ppm)	Zn (ppm)	As (ppm)	Rb (ppm)	Mo (ppm)	Ag (ppm)	Sn (ppm)	Cs (ppm)	Ce (ppm)	W (ppm)	Pb (ppm)	Bi (ppm)
0.66	160	12	610	27	160	<4	<4	<110	87	7	<13	160	7
0.28	79	<29	530	12	120	1	<6	<110	90	4	<14	130	<4
0.13	260	100	600	36	130	<2	<9	<130	100	<5	9	150	7
0.14	250	100	560	40	130	3	<9	<150	130	<4	28	190	7
0.72	46	<18	1,100	9	240	2	<3	<73	160	7	8	330	9
0.26	<17	2	380	3	87	1	<1	<21	45	2	6	110	3
0.15	160	76	310	22	60	1	<5	<67	46	2	<8	92	4
0.36	240	120	550	26	110	1	<5	<74	49	1	<10	170	5
0.08	130	43	210	15	53	2	<9	<150	59	5	5	78	<5
0.28	<150	<34	740	13	150	<6	<7	<72	87	3	<11	210	7
0.76	<120	6	1,200	11	270	<3	<10	<170	160	6	<13	320	10
0.74	260	<87	900	26	220	7	<17	<340	26	<8	23	160	8
0.77	300	<160	960	46	200	5	<48	<940	26	<15	22	190	10
0.38	190	116	680	23	260	5	<7	<120	51	<2	13	130	6
0.20	220	<20	750	18	730	5	<5	<82	64	<2	6	120	5
0.66	210	41	810	39	320	6	<17	<340	73	<6	18	210	6
0.30	<36	110	340	<24	1,100	47	n.a.	<100	60	12	<10	100	3
0.26	<66	310	630	<21	580	88	n.a.	<98	76	6	14	210	3
0.90	45	33	1,000	6	950	160	n.a.	22	80	14	45	310	5
0.35	<260	<88	350	<60	1,100	47	n.a.	<290	86	20	<30	77	<5
0.33	<220	1,900	620	<62	870	55	n.a.	<360	170	<8	<23	200	<7
0.56	<160	<62	1,100	<48	1,500	150	n.a.	<240	160	8	29	350	4
0.45	990	34	780	200	800	4	<13	<160	520	<4	50	160	24
0.66	1,300	3,500	1,300	290	760	6	11	<360	970	<9	49	190	23
0.36	1,100	2,300	760	200	430	3	7	<430	900	<9	33	150	18
0.33	780	8	550	140	450	31	<12	<230	700	1	57	100	15
0.11	1,300	17	820	350	340	<6	<15	<260	750	<6	<25	230	2
0.76	870	33	1,400	210	1,000	65	<27	<480	950	4	72	280	24
0.28	630	390	20	220	910	48	<21	<420	280	<11	130	96	12
0.26	480	410	420	77	540	26	<7	<140	130	<4	48	120	9
0.39	540	1,500	570	76	930	28	<14	<230	58	<10	43	120	10
0.77	700	2,600	940	130	1,600	46	<43	<320	250	<9	79	240	20
0.49	580	530	330	140	380	20	<30	<290	200	<8	<29	120	10
0.45	450	1,800	520	80	390	23	2	<80	180	1	53	120	9
0.24	490	1,600	530	88	430	26	1	17	210	1	10	120	8
0.18	430	910	740	98	580	26	1	9	220	1	42	130	9
0.60	1,300	58	1,100	260	160	150	<8	<160	240	<4	61	130	21
1.29	1,100	90	740	390	270	270	<12	<250	360	4	110	200	36
0.39	280	17	820	36	95	<8	<21	<320	22	<10	<28	73	<8
0.16	230	21	730	36	61	<3	<12	<150	26	<3	<17	100	2
1.30	270	22	550	42	96	5	<5	<130	28	16	7	100	4
0.16	260	180	990	35	130	<11	<18	<300	76	14	<36	170	<7
<0.04	99	<10	450	33	110	1	<3	<49	35	1	<4	190	<1
0.99	150	17	1,300	71	46	8	<4	<86	36	<2	<13	200	<4
0.27	290	5	1,100	21	140	<1	<2	<37	52	<1	<5	210	3
0.17	280	<14	1,300	48	89	4	1	<45	77	<1	<6	230	<2
0.08	340	<36	1,800	54	140	<4	<7	<110	98	<4	<14	310	<3
<0.03	440	<9	2,400	79	150	<1	2	<38	130	<1	<5	410	<1

[2]Calculated from clathrate melting point using ICE software (Bakker, 1997)
[3]Minimum concentration of CO_2 neccessary to form clathrates (in the simple H_2O-CO_2 system; Hedenquist and Henley, 1985)

estimated entrapment pressure of ~100 MPa, the solubility of H_2O in the silicate melt is ~4 wt % (e.g., Holtz et al., 2001), which requires a fluid/melt partition coefficient >25 to result in depletion of the corresponding element in the residual silicate melt during open-system, fluid-saturated magma crystallization (assuming 100% incompatibility of this element with respect to the crystallizing solids). The fluid/melt partition coefficient of Mo (2.4 ± 1.8) is significantly below this threshold value, implying that the Mo concentration in the residual melt should have increased with increasing degree of crystallization (unless significant amounts of Mo were incorporated into the crystallizing minerals). This prediction is in agreement with the compositional evolution shown in Figure 3B. In contrast, Cu concentrations in the melt inclusions show

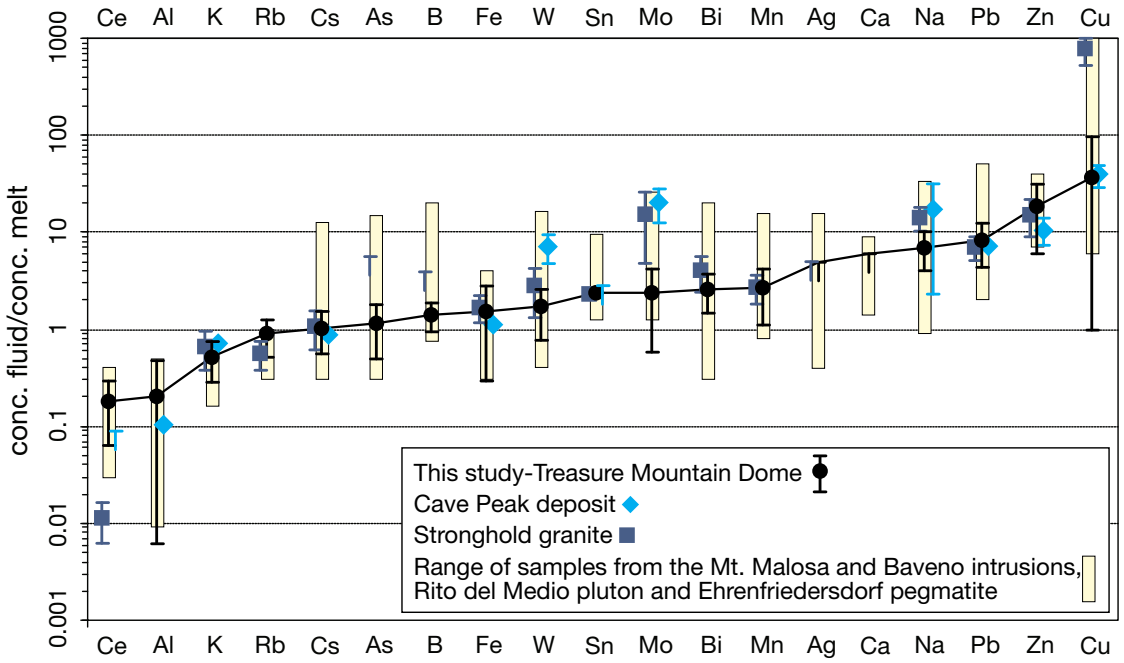

FIG. 5. Fluid/melt partition coefficient determined on coexisting fluid and melt inclusions in the Treasure Mountain dome compared to similar data obtained from the Mo deposit at Cave Peak (Texas; Audétat, 2010), the Stronghold granite (Arizona; Audétat et al., 2008), and four other granites (Zajacz et al., 2008): Mount Malosa (Malawi), Baveno (Italy), Rito del Medio (New Mexico), and Ehrenfriedersdorf (Germany). In cases where element concentrations in the fluid or in the melt were below the detection limit, corresponding maximum partition coefficients are indicated by truncated error bars. Error bars express 1σ standard deviations.

only a slight (if any) increase with increasing degree of fractionation (2–11 ppm in TM 7, 1–15 ppm in TM 2, and 3–30 ppm in TM 10 and TM 12), which is compatible with its high fluid/melt partition coefficient ($D_{Mo}^{fluid/melt}$ = 37.4 ± 60.3).

Drammen granite

A total of 20 melt inclusions were analyzed from the Drammen granite. Six of them were analyzed in two euhedral quartz crystals from miarolitic cavity Nr. 6 (samples Dra 6A and Dra 6B), and the remaining 14 inclusions along a 2-cm-long transect through the border of another cavity (sample Dra 2). This transect extends from fine-grained aplite over a pegmatitic contact zone into a euhedral quartz crystal. In all samples, the melt inclusions were coarsely crystallized and were chosen according to the criteria described in the previous section. As internal standard for LA-ICP-MS analyses, we used the average Al_2O_3 content of the two most evolved whole-rock analyses of quartz-feldspar porphyry reported in Ihlen et al. (1982). The results suggest that the melt inclusions are rhyolitic in composition (Table 2). A comparison of our melt inclusion data with whole-rock analyses reported from various textural facies of the Drammen granite is shown in Figure 6. The melt inclusion data nicely continue the trends displayed by the whole-rock data, suggesting that they are part of the same magma evolution. Although Cs clearly was less compatible than Rb in this granite also (Table 2; Cs increases by two orders of magnitude as Rb doubles), we plotted everything against Rb to be able to include the whole-rock data from the literature. Molybdenum and W concentrations generally increase with increasing degree of melt fractionation (from <10 ppm Mo and <5 ppm W at <500 ppm Rb to ~30 ppm Mo and ~30 ppm W at ~1,200 ppm Rb), except for a few extremely evolved melt inclusions analyzed in miarolitic quartz, which are strongly depleted in Mo. The three anomalously high Mo concentrations in the whole-rock data of medium- to fine-grained granite and quartz-feldspar porphyry (Fig. 6D) probably reflect minor hydrothermal mineralization. Along the transect through the border of miarolitic cavity Dra 2, Rb, Cs, and W concentrations continuously increase from melt inclusions analyzed in the aplite to those analyzed in euhedral quartz crystals, whereas Mo concentrations first increase and then dramatically decrease in the most evolved melts analyzed. The latter reflects either efficient Mo extraction by fluids or incorporation of Mo in crystallizing solids. The presence of molybdenite inclusions in the euhedral quartz crystals points to the second explanation and suggests that, at the very last stages of magma solidification, perturbations in P, T, f_{S_2}, and/or f_{O_2} may have led to wholesale molybdenite precipitation.

The fluid evolution recorded in the miarolitic cavities of the Drammen granite is principally the same as the one in the Treasure Mountain dome, starting with intermediate-density (0.6–0.7 g/cm^3), partly CO_2 bearing fluid inclusions with salinities of 4.4 to 6.3 wt % NaCl equiv (corresponding to the TypeA-II inclusions described in Olsen and Griffin, 1984), then passing through a stage in which the fluid was two phase, and finally reaching a state where aqueous, high-density fluid inclusions were trapped. However, in the samples of the Drammen granite, the proportion of intermediate-density fluid inclusions to subsequent vapor and brine

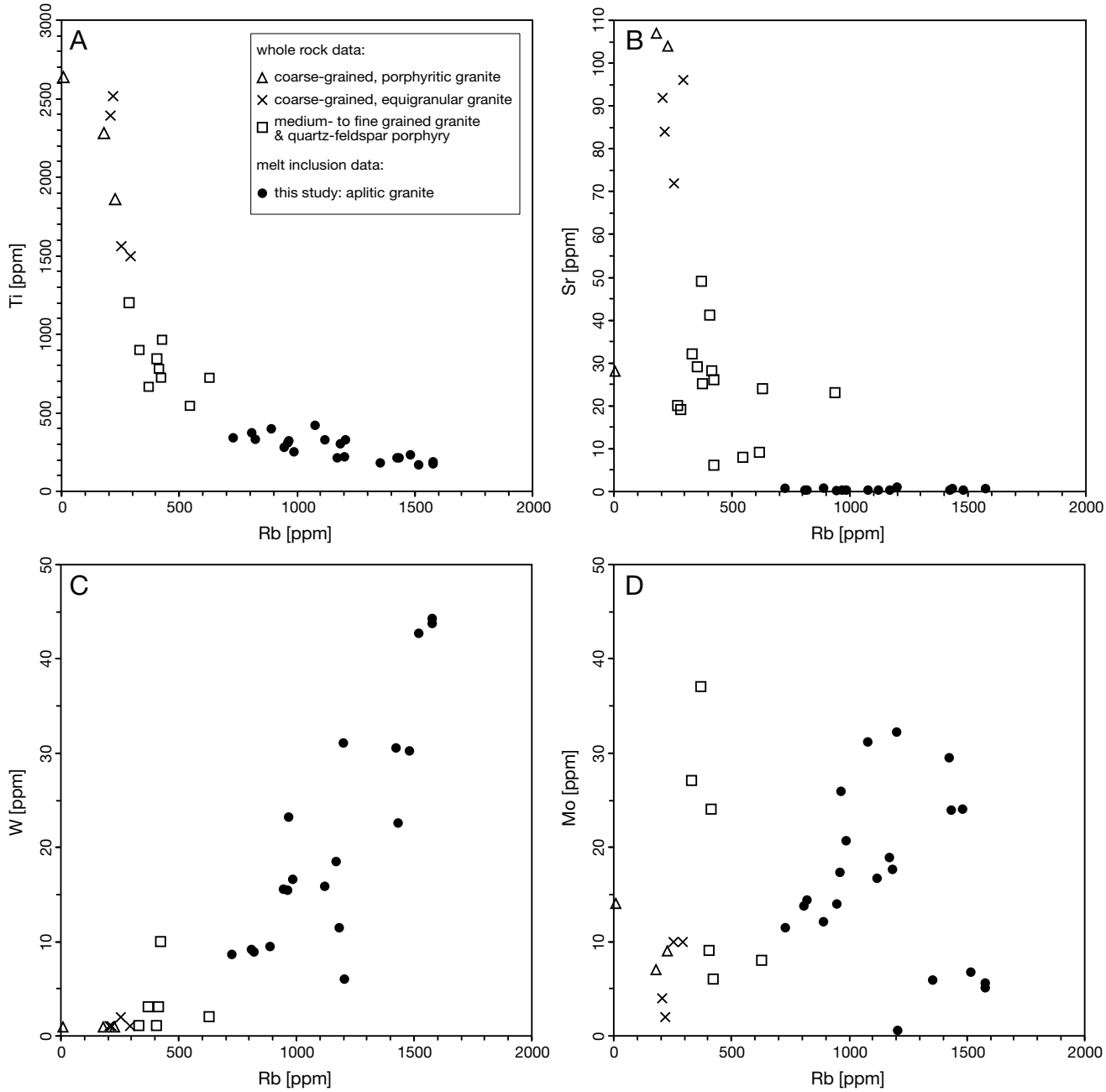

FIG. 6. (A-D) Compositional evolution of melt inclusions (black dots) and whole rocks (open symbols and crosses) of the Drammen granite. Whole-rock data are from Ihlen et al. (1982) and Trønnes and Brandon (1992). In this case, we use Rb as an indicator of melt fractionation because there are no Cs data available for the whole rocks. Titanium and Sr decrease with increasing degree of melt fractionation, whereas W and Mo generally increase, except for some extremely evolved melts trapped in miarolitic quartz that were strongly depleted in Mo.

inclusions is much larger, and the immiscibility gap recorded by vapor and brine inclusions is much smaller. Brines with salinities greater than ~35 wt % NaCl equiv are conspicuously absent in our samples. This suggests that the Drammen granite solidified at significantly higher pressure than the Treasure Mountain dome, which is in accord with conditions of ~680°C/140 MPa reconstructed from the intersection of intermediate-density fluid inclusion isochores (~5.7 wt % NaCl equiv, Th_{tot} ~425°C) with the granite solidus, and with pressure estimates of 130 to 150 MPa reported by Olsen and Griffin (1984) and Larsen et al. (2009). CO_2 concentrations in these intermediate-density fluid inclusions were mostly too low to result in clathrate formation upon cooling (implying that CO_2 concentrations were below 1.6 mol %; Hedenquist and Henley, 1985), but in some inclusions of sample Dra 6 clathrates with melting temperatures indicating CO_2 concentrations up to 2.4 mol % were observed. Sulfur concentrations measured by LA-ICP-MS range from 0.2 to 0.5 wt % (Table 1).

Solid inclusions identified within quartz crystals from miarolitic cavities include topaz, muscovite, albite, K-feldspar, and molybdenite on early growth zones (which are contemporary to slightly younger than the analyzed melt inclusions), and tourmaline, epidote, chlorite, hematite, and galena on later growth zones.

Molybdenum concentrations in intermediate-density fluid inclusions range from 3 to 270 ppm, with the majority of values measured in Al-rich (i.e., high-temperature) inclusions clustering around 30 to 40 ppm Mo (Table 3). Copper concentrations show a large scatter, ranging from 8 to 3,500 ppm without any apparent relationship to other elements. Although roughly contemporaneous, none of the analyzed fluid and melt inclusions were unambiguously coexisting, for which reason we did not calculate fluid/melt partition coefficients. However, average Mo concentrations in melt and fluid inclusions of sample Dra 6 (20 ± 5 ppm vs. 30 ± 11 ppm, respectively) imply a $D_{Mo}^{fluid/melt}$ value of 1.5 ± 0.9, which agrees within error with the value of 2.4 ± 1.8 determined in the Treasure Mountain dome. Both $D_{Mo}^{fluid/melt}$ values are far below the threshold value that would be required for a net depletion of Mo in the residual silicate melt during fluid-saturated crystallization of the Drammen granite (~20, corresponding to a water solubility of ~5.0 wt % at 150 MPa/700°C).

Glitrevann granite

Due to the limited number of suitable samples found in this granite, we can provide only preliminary data. Four coarsely crystallized melt inclusions were analyzed in quartz grains of the aplitic granite surrounding the two miarolitic cavities Glt 2 and Glt 3. As internal standard for the quantification of the LA-ICP-MS measurements we used the average Al content of whole-rock analyses of this facies reported in Jensen (1985). The least evolved melt inclusion (Glt 2, MI2) is compositionally similar to the most evolved whole-rock composition reported by Jensen (1985), whereas the other three melt inclusions record slightly higher degrees of fractionation (Table 2). Molybdenum concentrations are reproducible at 12 ± 1 ppm.

Euhedral quartz crystals from the miarolitic cavities contain a high proportion of coexisting vapor and brine inclusions, with late-stage brine inclusions reaching salinities of up to 80 wt % NaCl equiv. Intermediate-density fluid inclusions are rare and restricted to the base of the crystals, whereas aqueous, high-density fluid inclusions occur mostly in the upper portion of the crystals. Solid inclusions comprise muscovite, feldspar, gypsum, monazite, rutile, and molybdenite along early growth zones, and muscovite, feldspar, rutile, monazite, and tourmaline along later growth zones. No melt inclusions were found. Intermediate-density fluid inclusions have densities of 0.6 to 0.7 g/cm^3 and salinities of 6.7 to 8.1 wt % NaCl equiv, and contain between 2.1 and 3.5 mol % CO_2, as revealed by melting temperatures of ice and clathrates. LA-ICP-MS analyses of 10 such fluid inclusions reveal S concentrations in the order of ~0.5 wt % and rather low Mo concentrations of ~5 ppm (Table 3). The fact that none of these inclusions contain more than 1,100 ppm Al suggests that they probably do not represent magmatic fluids but were trapped at subsolidus conditions (most likely between 600° and 700°C). Therefore, they are comparable to the Mo-poor intermediate-density fluid inclusions measured in samples TM 5 and TM 10 of Treasure Mountain.

Reequilibration of fluid inclusions from the Drammen granite

Recent experimental reequilibration studies on both natural and synthetic fluid inclusions (e.g., Mavrogenes and Bodnar, 1994; Li et al., 2009; Zajacz et al., 2009; Lerchbaumer and Audétat, 2012b) revealed that the Cu (as well as Na, H, Ag) content of quartz-hosted fluid inclusions can easily be modified by diffusion after fluid entrapment. This process seems to be particularly efficient when S-bearing, acidic fluid inclusions are reequilibrated in a more neutral fluid (Lerchbaumer and Audétat, 2012b). In this case, H^+ diffuses out of the acidic fluid inclusions through the host quartz into the surrounding, less acidic fluid. To maintain charge balance, small, single-charged ions like Cu^+, Na^+, and Ag^+ diffuse from the outer fluid into the fluid inclusions. Whereas the diffusion of Na^+ stops once its concentration within the fluid inclusion becomes significantly higher than in the outer fluid, incoming Cu^+ combines with the S present within the fluid inclusion to precipitate as Cu sulfide. Copper concentrations in fluid inclusions can increase by more than one order of magnitude in this manner (Lerchbaumer and Audétat, 2012b).

In view of these results, the question arises of whether the Cu contents of the natural fluid inclusions discussed above are reliable. Two lines of evidence indicate that this may not be the case: (1) in all three occurrences, acidic and S-bearing fluids were trapped at magmatic conditions and were later replaced by less acidic fluids, and (2) Cu concentrations measured within well-defined fluid inclusion populations are far less reproducible than the concentrations of other elements. To test whether Cu has been gained we reequilibrated a fluid inclusion trail of sample Dra 6B (trail A) in an acidic surrounding fluid at its estimated entrapment conditions of ~650°C and ~140 MPa for 22 days. The fluid contained 6.3 wt % NaCl, 3.2 wt % KCl, 0.6 wt % S, 620 ppm Rb, 340 ppm Cs, and 0.4 mol/kg$_{solution}$ HCl. Copper and Mo were added in excess amounts (i.e., more than what can be dissolved during the run) in the form of chalcopyrite and molybdenite, respectively, whereas albite, muscovite, orthoclase, and topaz were added to buffer the pH at a low value. The latter was confirmed by the low pH (≤0.3) measured in the quench solution after the experiment. A similar reequilibration experiment performed on coexisting vapor and brine inclusions in a natural quartz sample from the Erongo granite (Namibia) is described in Lerchbaumer and Audétat (2012b). Details regarding the composition of fluid inclusions on trail A (Dra 6B) before and after reequilibration are given in Table 4, together with the composition of fluid inclusions that trapped the outer fluid during reequilibration. Comparison of element concentrations in fluid inclusions on trail A before and after equilibration (Fig. 7) reveals that, within analytical uncertainty, only the concentrations of Na, Rb, and Cs changed significantly. Sodium concentrations decreased by about a factor of three, whereas Rb and Cs concentrations increased by about a factor of two. Copper concentrations decreased from 1,200 ± 600 to 770 ± 190 ppm and became much more reproducible, suggesting that some of the fluid inclusions may have experienced

TABLE 4. LA-ICP-MS Data of Fluid Inclusions Before and After Equilibration (sample Dra 6B, trail A)

	Dra 6B, trail A		
Fluid composition	6.3 wt % NaCl, 3.2 wt % KCl, 0.6 wt % S, 0.4 mol/kg$_{solution}$ HCl, 620 ppm Rb, 340 ppm Cs		
Mineral buffers	Ccp, Mo, Ab, Ms, Or, Toz		
P [MPa]/T [°C]	650/140		
t [days]/pH[1]	22/<0.3		
	Before equilibration (n = 4)	After equilibration (n = 5)	Newly formed inclusions (n = 5)
Salinity (wt % NaCl equiv)	5.7 ± 0.2	5.5 ± 0.1	12.8 ± 1.0
Na (wt %)	*1.64 ± 0.17*	0.49 ± 0.09	2.17 ± 0.14
Al (wt %)	0.23 ± 0.17	0.15 ± 0.08	0.36 ± 0.40
S (wt %)	0.25 ± 0.07	<0.39	<5.10
Cl (wt %)	5.19 ± 1.79	4.60 ± 0.44	<25.0
K (wt %)	1.24 ± 0.13	1.39 ± 0.33	1.32
Ca (wt %)	<2.97	<5.90	n.a.
Mn (wt %)	0.17 ± 0.12	0.16 ± 0.07	0.006
Fe (wt %)	0.34 ± 0.15	0.31 ± 0.13	0.97 ± 0.18
B (ppm)	490 ± 69	380 ± 100	<1,300
Cu (ppm)	1,200 ± 600	770 ± 190	5,600 ± 410
Zn (ppm)	530 ± 170	400 ± 120	<1,900
As (ppm)	100 ± 30	70 ± 20	<340
Rb (ppm)	450 ± 90	1,100 ± 380	560 ± 40
Mo (ppm)	24 ± 3	21 ± 6	10
Ag (ppm)	2 ± 1	1 ± 0.4	<46
Sn (ppm)	13 ± 6	<290	<6,000
Cs (ppm)	200 ± 18	420 ± 190	*340*
Ce (ppm)	1.03 ± 0.08	1.3 ± 0.21	<18
W (ppm)	35 ± 22	38 ± 12	<90
Pb (ppm)	120 ± 4	*120*	<400
Bi (ppm)	9 ± 1	7 ± 2	<38

Notes: Italic numbers mark elements that were used as interal standard; element concentrations without standard deviation are based on only one measurement; errors are within 1σ standard deviation; Ab = albite, Ccp = chalcopyrite, Mo = molybdenite, Ms = muscovite, n.a. = not analyzed, Or = orthoclase, Toz = topaz

[1] Quench pH measured after the run

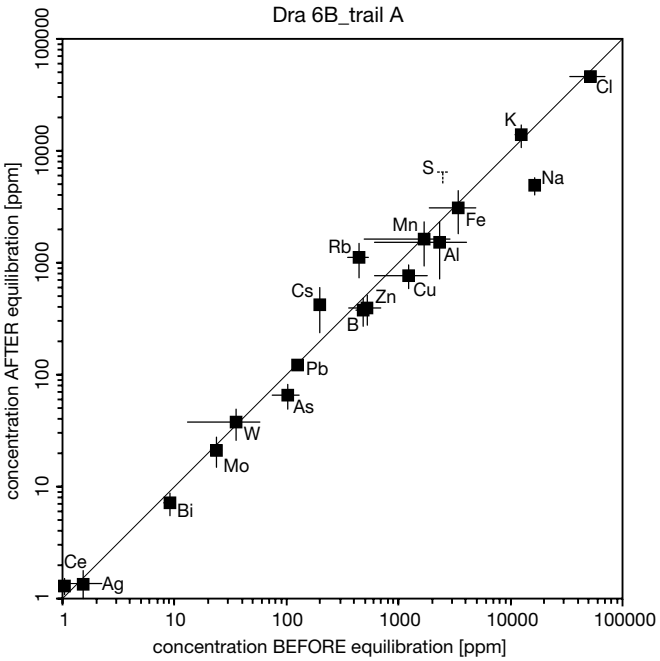

FIG. 7. Element concentrations in fluid inclusions on trail A of sample Dra 6B from the Drammen granite, before and after reequilibration at 650°C, 140 MPa. Error bars express 1σ standard deviations. Notice the significant changes in Na, Rb, and Cs concentrations, whereas all other element concentrations stayed the same within analytical uncertainty.

postentrapmental Cu gain. However, compared to the experiments described in Lerchbaumer and Audétat (2012b), the change in Cu concentrations observed in the present experiment was small. This may be a consequence of the fact that the fluid inclusions on trail A contained much less sulfur (~0.3 wt % S) than those reequilibrated by Lerchbaumer and Audétat (2012b; 1–2 wt % S). Other fluid inclusions analyzed from Treasure Mountain, Drammen, and Glitrevann have similarly low S contents (Tables 1, 3). It is thus possible that the Cu concentrations listed in Tables 1 and 3 are in the correct order of magnitude, although the large scatter within single fluid inclusion trails remains worrisome. The same argument applies for Bingham whereas, for Questa, Cave Peak, Butte, and El Teniente, predictions are even more difficult to make because no S concentration data are available.

In principle, the Cu content of the melt inclusions could also have been affected by postentrapmental diffusion (Kamenetsky and Danyushevsky, 2005; Zajacz et al., 2009). However, the values are very low (mostly <10 ppm) and fairly reproducible, for which reason we consider them to be real.

Comparison with Data from Other Intrusions

Molybdenum concentrations in silicate melts

The Mo-mineralizing potential of granitic intrusions depends on many factors, including (e.g., Keith et al., 1993) (1) the metal content of the silicate melt from which the mineralizing fluids exsolved, (2) the metal content of these fluids (which may not simply reflect the metal content of the melt if fluid-melt partition coefficients are highly variable), (3) the degree of fluid (and/or melt) focusing, (4) the size and shape of the magma chamber, (5) the abundance of volatiles in the magma, and (6) the efficiency of Mo precipitation from the magmatic-hydrothermal fluids. The following is an attempt to compare the first four of these variables in economically Mo mineralized intrusions, subeconomically Mo mineralized intrusions, barren intrusions, and porphyry Cu-Mo–mineralized intrusions. Due to the limited amount of available data, the results have to be regarded preliminary.

Molybdenum concentrations in silicate melts from various mineralized and barren intrusions are shown in Figure 8. Because whole rocks do not reliably record original metal contents of melts and magmas (e.g., White et al., 1981; Keith et al., 1993), we exclusively rely on melt inclusion data for this purpose, remembering that, in the case of closed-system fractional crystallization, melt inclusions represent snapshots in time whereas whole rocks represent the integrated products. As an index of the degree of melt fractionation we use Cs, which is one of the most incompatible trace elements in silicic magmas (e.g., Audétat and Pettke, 2003) and can easily be analyzed by LA-ICP-MS because it is a heavy, monoisotopic element free of interferences. In most magmas, Cs behaves

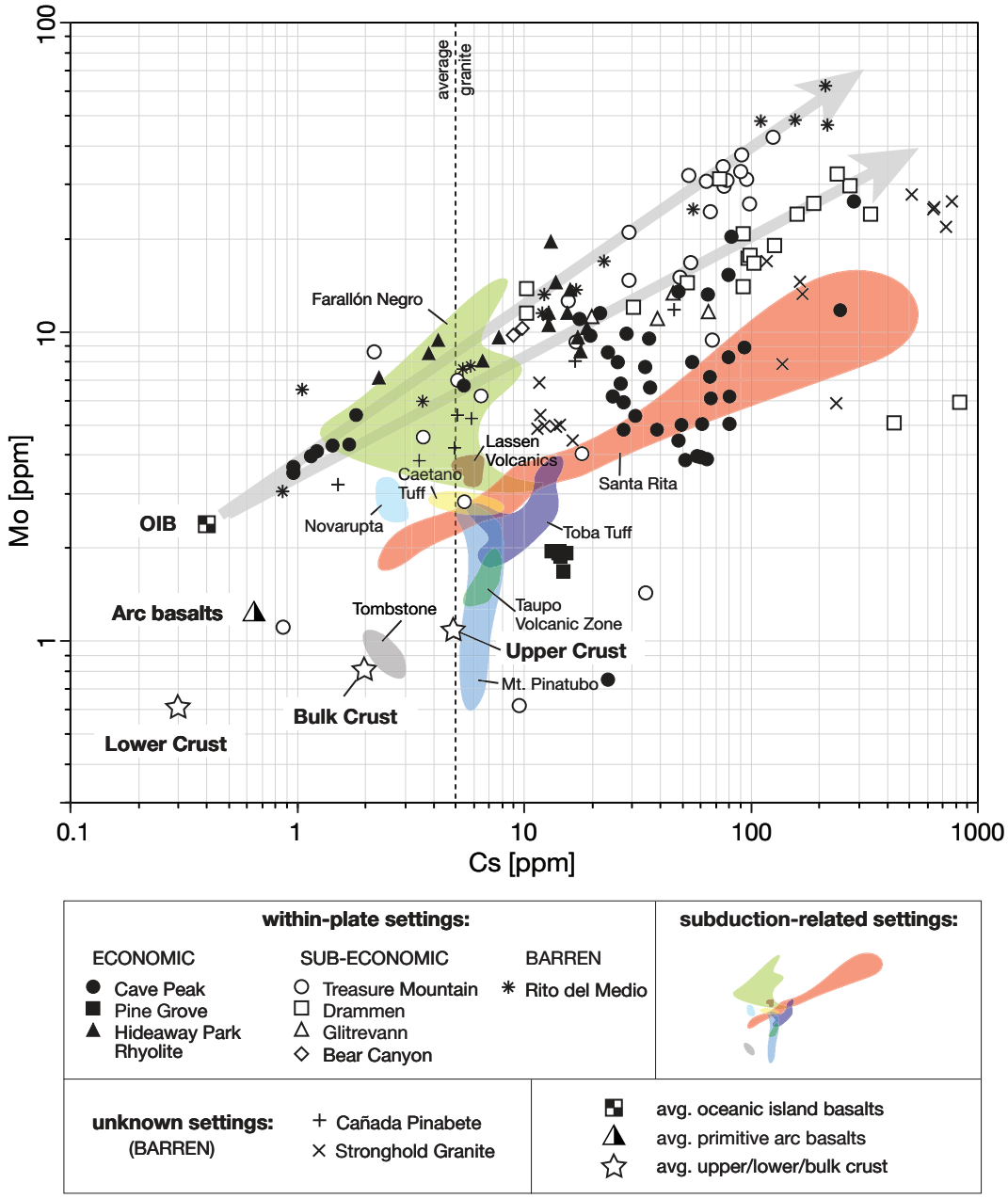

FIG. 8. Molybdenum versus Cs concentrations of melt inclusions from Mo- and Cu-mineralized granites and porphyries, sorted according to their economic relevance and tectonic setting. Notice the generally lower Mo/Cs ratios of subduction-related melts compared to melts from within-plate settings. Sources of data: Cave Peak: Audétat (2010); Pine Grove: Audétat et al. (2011); Hideaway Park rhyolite: personal communication with Celestine Mercer (2012); Treasure Mountain, Drammen, Glitrevann: this study; Bear Canyon: Audétat et al. (2011); Stronghold granite: Audétat et al. (2008); Cañada Pinabete: Audétat et al. (2011); Rito del Medio: Audétat et al. (2008); Farallón Negro: Halter et al. (2004b); Lassen Volcanics, Caetano Tuff, Novarupta, Toba Tuff, Taupo Volcanic Zone, Tombstone: Audétat et al. (2011); Santa Rita: Audétat et al. (2004, 2011); Mt. Pinatubo: Borisova et al. (2008); average oceanic island basalt: Sun and McDonough (1989); average primitive arc basalts: GEOROC database; specific references are given in Bali et al. (2012); average upper/lower/bulk crust: Rudnick and Gao (2003); average granite: Taylor (1964).

about twice as incompatibly as Rb (e.g., Table 2, references in Table 6). Taylor (1964) estimated the Cs and Rb contents of average granite at 5 and 150 ppm, respectively.

For further discussion, the data are divided into subduction-related and within-plate magmas. Climax-type porphyry Mo deposits are associated with within-plate magmas, whereas porphyry Cu (± Mo, Au) deposits are associated with subduction-related magmas (e.g., Carten et al., 1993; Sillitoe, 2010; Richards, 2011). For a given Cs content, within-plate magmas (Treasure Mountain, Drammen, Glitrevann, Bear Canyon, Cave Peak, Pine Grove, Hideaway Park, Rito del Medio) generally contain more Mo than subduction-related magmas

(Santa Rita, Alumbrera/Farallón Negro, Mt. Pinatubo, Taupo Volcanic Zone, Toba Tuff, Lassen volcano, Tombstone, Novarupta, Caetano Tuff) (Fig. 8). Exceptions are found in some melts analyzed from the subduction-related Farallón Negro Complex, which are enriched similarly to average within-plate magmas, some melts analyzed from Cave Peak, and those analyzed from Pine Grove, which have a distinct within-plate trace element signature (Audétat et al., 2011) but very low Mo/Cs ratios. The latter two samples, however, show evidence for magmatic molybdenite saturation (Audétat et al., 2011), which means that the Mo content of the bulk magma could have been much higher than the Mo concentrations recorded in the melt inclusions. The tectonic settings of the Stronghold granite and the Cañada Pinabete pluton are not clear. It is interesting to note that, with the exception of the molybdenite-saturated melts mentioned above, the trends of the melt inclusions analyzed from within-plate settings (gray arrows) project back to the average composition of oceanic island basalts (OIB), which suggests that the Mo is derived from the mantle (Audétat et al., 2011). Melts produced by melting of average crustal reservoirs would be expected to lie on trends that start at the corresponding stars in Figure 8 and have slopes similar to the gray arrows, which results in distinctly lower Mo/Cs values than observed in the melt inclusions. Similarly, most melt inclusions analyzed from subduction-related settings lie on a trend that projects back to the average composition of primitive arc basalts (Farallón Negro, Mt. Pinatubo, and Tombstone being exceptions). Although, in this case, the Mo/Cs ratios are closer to those expected for crustal melts, this implies that Mo may have been derived from the mantle also in subduction-related settings. This interpretation is supported by Pb isotope data of fluid inclusions, suggesting that the metals contained in major porphyry Cu and porphyry Mo deposits of the United States are derived from ancient subcontinental lithosphere (Pettke et al., 2010).

Looking at the data from within-plate magmas only, there seems to be no systematic difference between economically Mo mineralized granites (Cave Peak, Pine Grove, Hideaway Park rhyolite), subeconomically Mo mineralized granites (Treasure Mountain, Drammen granite, Glitrevann granite, Bear Canyon pluton), and the barren Rito del Medio pluton. Except for Pine Grove, all samples define trends that pass through ~10 ppm Mo at ~10 ppm Cs and have a slope of 0.5 or smaller in a corresponding log-log diagram (meaning that Mo is distinctly more compatible than Cs). This suggests that economic porphyry Mo deposits formed from melts that were not fundamentally different from melts occurring in other intrusions in within-plate settings. However, what appears to have varied is the size of the magma chamber and the efficiencies of residual melt extraction and fluid focusing (see below).

Melt inclusions analyzed from subduction-related intrusions have generally lower Mo contents than similarly evolved melts analyzed from within-plate settings, except for the data from the Farallón Negro Complex. For example, at a Cs concentration of 10 ppm (~320 ppm Rb), Mo concentrations in subduction-related melts are about 2 to 5 ppm, whereas in within-plate melts they are about 7 to 16 ppm (Fig. 8). In some subduction-related magmas (Alumbrera/Farallón Negro, Santa Rita) the slopes of the fractionation trends are similar to the ones observed in within-plate magmas, whereas in other subduction-related magmas (Toba Tuff, Taupo Volcanic Zone, Mt. Pinatubo) they are much steeper, suggesting that Mo behaved as incompatibly as Cs.

Metal concentrations in magmatic fluids

Molybdenum concentrations in fluid inclusions that are representative of (near-) magmatic, single-phase fluids are compiled in Figure 9. In the case of Santa Rita, where no such fluid inclusions have been identified, we used the composition of vapor inclusions trapped at ~720°C near the crest of the immiscibility field. Although the data are much more scattered than in Figure 8, the general trends appear to be the same. At any given Cs content, maximum Mo concentrations in porphyry Mo-related fluids (Cave Peak, Questa) are similar to those observed in fluids from subeconomically mineralized (Treasure Mountain, Drammen granite) and barren (Rito del Medio pluton) intrusions in within-plate settings, but are higher than those in porphyry Cu (Mo)-related fluids (El Teniente, Butte, Santa Rita), except for Bingham. However, most fluid inclusions analyzed from Mo-mineralized granites have higher Cs and Mo contents (≥40 ppm Cs; ≥20 ppm Mo) than those analyzed from porphyry Cu(Mo) deposits (≤10 ppm Cs; ≤20 ppm Mo; see also Table 5), which reflects the more evolved character of melts in the former occurrences. Exceptions are the fluids at Bingham (Landtwing et al., 2010) and the low-Cs fluid population identified at Questa (Klemm et al., 2007). A different trend is displayed by Cu: average fluids in Mo-mineralized granites contained 600 to 2,100 ppm Cu, whereas average fluids in porphyry Cu (Mo)-mineralized intrusions contained 3,500 to 6,200 ppm Cu. Mo/Cu ratios in the fluids of Mo-mineralized granites were thus significantly higher than in those associated with porphyry Cu (Mo) deposits (Table 5, Bingham again being an exception). However, even in fluids from porphyry Mo deposits, absolute concentrations of base metals (600–1,200 ppm Cu, 300–1,400 ppm Zn, 200–400 ppm Pb) were many times higher than the concentration of Mo, which raises the question of where all these base metals went, because the ores are nearly free of base metals. A likely explanation is that Mo precipitation was highly selective, and that other metals, including Cu, precipitated at structurally higher levels. This interpretation is supported by the comparatively low Mo solubility in sulfur-bearing fluids (Zhang et al., 2012), the occurrence of both disseminated and vein-hosted Cu, Pb, and Zn mineralization above the porphyry Mo deposits at Redwell basin and Mt. Emmons (Sharp, 1978; Thomas and Galey, 1982), a change from Mo-dominated deposits in more deeply exposed areas to Cu-Au-Pb-Ag-Zn deposits in less uplifted portions along the southern margin of the Questa caldera (Clark and Read, 1972; Jones, 1990), and the fact that both the Climax and Urad orebodies were already partly eroded, but it is at odds with the lack of base metal mineralization in the ~1.3- and ~1.1-km sections preserved above the orebodies at Henderson and Pine Grove, respectively. In their study on Questa, Klemm et al. (2008) proposed that the lack of base metal mineralization at the porphyry level is due to a low concentration of reduced sulfur in the input fluid or in the mineralizing brine after boiling off an S-rich vapor phase. Similarly,

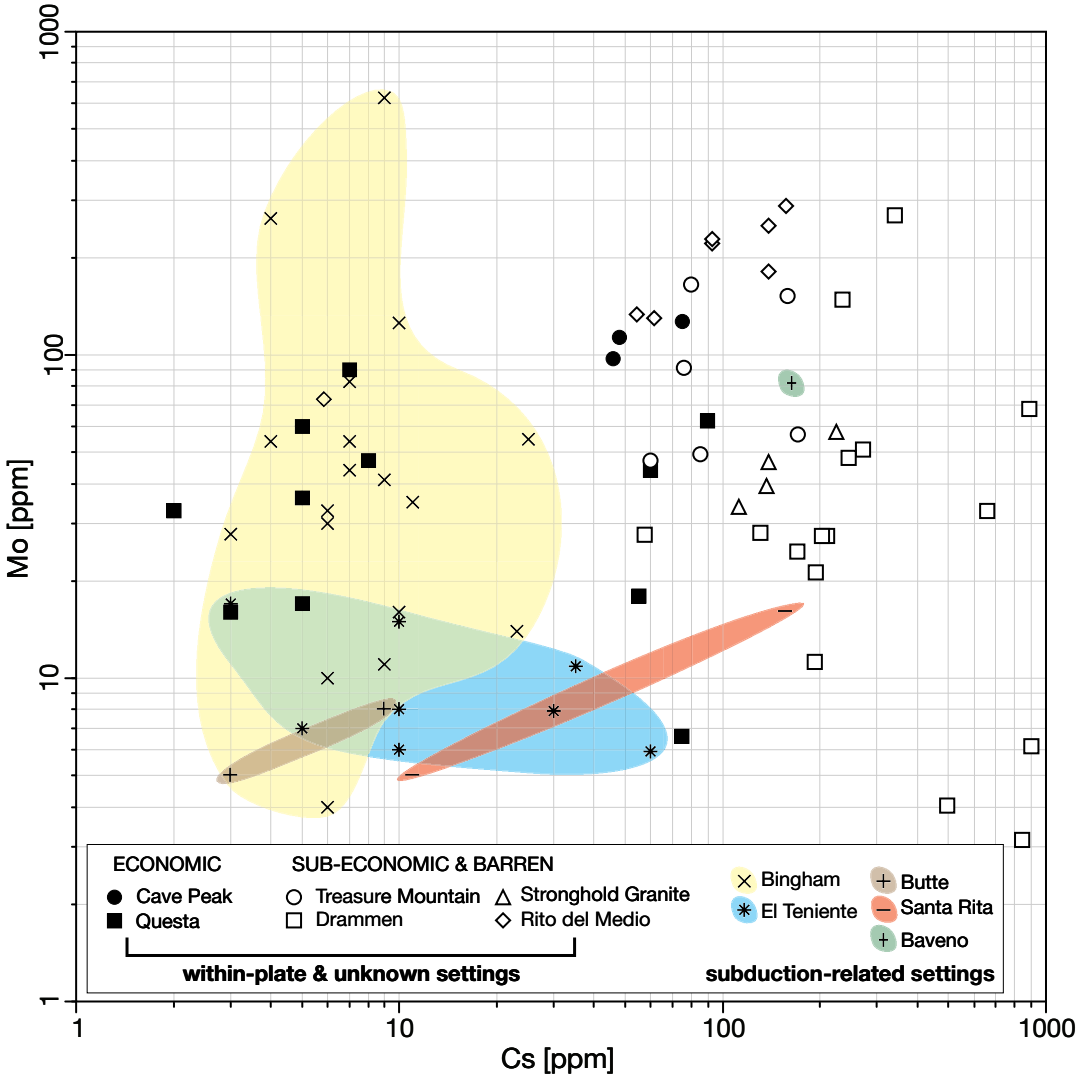

FIG. 9. Molybdenum versus Cs concentrations in fluid inclusions from Mo- and Cu-mineralized granites and porphyries, sorted according to their economic relevance and tectonic setting. Sources of data: Cave Peak: Audétat (2010); Questa: Klemm et al. (2008); Treasure Mountain, Drammen: this study; Stronghold granite, Rito del Medio: Audétat et al. (2008), Zajacz et al. (2008); Bingham: Landtwing et al. (2010); El Teniente: Klemm et al. (2007); Butte: Rusk et al. (2008); Santa Rita: Audétat et al. (2004, 2011); Baveno: Zajacz et al. (2008).

Seo et al. (2012) concluded from a recent study on Bingham that selective precipitation of Mo vs. Cu + Fe was controlled by redox potential and fluid acidity. It needs to be noted that the pressure and temperature ranges of Mo precipitation recorded by fluid inclusions in the breccia bodies at Questa (Klemm et al., 2008; 420°–360°C/~20 MPa) and Cave Peak (Audétat, 2010; 450°–550°C/~50 MPa), and in the stockwork at Bingham (Seo et al., 2012; 580°C/71 MPa) are significantly lower than what has been observed in the samples examined in this study and what can be inferred from the distribution of Mo at other locations. Samples investigated in this study show a large decrease in the Mo content from the earliest, clearly magmatic fluids to slightly later, but still >600°C (based on the salinity of subsequent brines), intermediate-density fluids. Evidence for Mo precipitation at near-magmatic temperatures in porphyry Mo deposits includes (1) the fact that ore shells typically straddle the parental intrusions, (2) the presence of molybdenite-bearing vein dikes showing a continuum between magmatic and hydrothermal textures (White et al., 1981), and (3) the presence of primary molybdenite in unidirectional solidification textures (Carten et al., 1988; Sinclair, 2007). More work is needed to constrain the conditions of molybdenite precipitation and their relationship to the conditions of base metal precipitation.

Overall, the range of Mo concentrations measured in single-phase, premineralization fluids from barren and productive intrusions is relatively small (~1.6 orders of magnitude; Fig. 9), suggesting that the Mo mineralization potential was, to a large extent, controlled by factors other than the metal content of the fluid.

Size, depth, and structure of magma chambers

These parameters are difficult to quantify because porphyry Mo mineralization typically forms within and around

TABLE 5. Overview on S, Cs, Mo, and Cu Concentrations in Magmatic Fluids from Mo-Mineralized Granites and Porphyry Mo and Porphyry Cu(Mo) Deposits

Sample no.	S (wt %)	Cs (ppm)	Mo (ppm)	Cu (ppm)	Pb (ppm)	Zn (ppm)	Mo/Cu in fluid	References
Within-plate occurrences								
TM 12A	0.6 ± 0.3[1]	100 ± 52	79 ± 58	620 ± 720	210 ± 110	670 ± 320	0.13 ± 0.18	This study
Dra 6A	0.4 ± 0.1[1]	230 ± 170	51 ± 18	1,170 ± 320	110 ± 10	340 ± 280	0.044 ± 0.040	This study
Questa	?	30 ± 33	37 ± 25	2,100 ± 1,600	280 ± 230	730 ± 560	0.042 ± 0.066	Klemm et al. (2007)
Cave Peak	?	56 ± 16	112 ± 13	620 ± 120	390 ± 50	1,400 ± 100	0.18 ± 0.02	Audétat (2010)
Subduction-related occurrences								
Butte	?	6 ± 4	7 ± 2	3,500 ± 1,800	20 ± 8	130 ± 40	0.004 ± 0.003	Rusk et al. (2004)
Bingham	0.7 ± 0.3[2]	9 ± 7	51 ± 36	6,200 ± 3,800	330 ± 90	600 ± 320	0.02 ± 0.02	Landtwing et al. (2010)
El Teniente	?	19 ± 18	8 ± 4	5,900 ± 4,000	80 ± 70	340 ± 280	0.002 ± 0.001	Klemm et al. (2007)

[1] Average of all fluid inclusions analyzed from this intrusion (not only TM 12A or Dra 6A)
[2] Vapor data in Seo et al. (2009)

small apophyses well above the main magma chamber; hence, the latter is usually not exposed. Nevertheless, first-order estimates of the magma volumes and theoretically available amounts of Mo in the magma systems mentioned above are provided in Table 6. For each mineralized system, a minimum magma volume required to form the observed Mo mineralization has been calculated from the estimated Mo content of its "average magma composition," an assumed extraction efficiency of 50%, and the total amount of Mo present in the orebody/orebodies. The Mo content of the average magma composition was estimated as follows: first, the least fractionated melt inclusion or whole rock (notice the fundamental difference between these two kinds of samples, as explained above) associated with mineralization was identified based on its Cs and/or Rb content, and then the corresponding Mo concentration was estimated based on the Cs-Mo trends shown in Figure 8. Of course, this definition of the average magma composition is associated with considerable uncertainty, but, without access to the large intrusions beneath porphyry-type ore deposits, it is all we can do. The results suggest that giant Mo deposits (here defined as ≥1 Mt Mo) required magma volumes of at least 100 km^3, whereas medium-sized (here defined as 0.1–1.0 Mt Mo) deposits required magma volumes of at least several tens of km^3. Similar results have been obtained in earlier studies: Wallace et al. (1968) calculated that 100 to 125 km^3 of magma was necessary to form the Climax orebodies, and Keith et al. (1993) argued that ≥150 km^3 was necessary to form the Henderson deposit.

For both mineralized and barren intrusions, an independent estimate on the amount of potentially available Mo may be obtained from the geologically constrained intrusion volume, its average composition, and the estimated Mo content of melts at this degree of melt fractionation. Three points have to be noted here: (1) we define the maximum rock volume that could have been partially molten at the time of (potential) Mo mineralization as "intrusion volume" (i.e., in large, composite batholiths like the Drammen granite, in which several intrusive phases crosscut each other, only the latest phases associated with Mo mineralization are considered), (2) in the absence of any constraints on the intrusion thickness we assume a minimum thickness of one-fourth of the lowest exposed dimension (i.e., for a granite exposed over an area of 4 × 6 km we assume a minimum thickness of 1 km), and (3) the total amount of Mo in the magma (third to the last column in Table 6) is listed without considering the efficiency of extraction, i.e., at an extraction efficiency of 50%, the amount of Mo ending up in a hypothetical deposit would be only half of the amount shown in this column.

A comparison between the calculated minimum magma volumes for economic Mo deposits (last column in Table 6) and the minimum magma volumes associated with subeconomic and barren intrusions (fifth column in Table 6) reveals that magma volumes of the Rito del Medio pluton, the Cañada Pinabete pluton, the Bear Canyon pluton, and Schieffelin granite (Tombstone) may have been simply too small to produce economic mineralization. The magma volumes of the Stronghold granite, the Treasure Mountain dome, the Drammen granite, and the Glitrevann granite, on the other hand, would have been large enough to produce at least a medium-sized Mo deposit. In these intrusions, factors other than magma chamber size appear to have prevented economic mineralization. An obvious candidate is the efficiency of Mo extraction from the magma, which depends to a large extent on the degree of fluid/melt focusing. With respect to this, it is interesting to note that whole rocks analyzed from the Drammen granite do not appear to be significantly depleted in Mo (Fig. 6), indicating that the lack of economic mineralization in this magma system may be due to inefficient Mo extraction. The degree of fluid/melt focusing depends on (1) the depth of intrusion, (2) the shape of the magma chamber, (3) the presence/absence of vent structures, and (4) the mode of magma crystallization. The mode of magma crystallization and the presence/absence of vent structures may be controlled by the frequency and magnitude of magma chamber recharge/reactivation by ascending mafic magmas (Bachmann et al., 2007; Walker et al., 2007). For example, a granitic magma that intrudes at 2- to 5-km depth and evolves as an essentially closed system may never form economic Mo mineralization because it reaches a mushy state relatively quickly, which prevents residual melts from accumulating in the upper parts of the magma chamber. In contrast, in a magma chamber that is periodically reheated by underplating mafic magmas, residual melts are able to rise and pool under the roof to form a crystal-poor rhyolitic cap (Bachmann et al., 2007; Walker et al., 2007). From this cap, dissolved volatiles

TABLE 6. Comparison of Magma Type, Magma Chamber Size, and

Occurrence	Geochemical signature	Depth at the top of magma chamber (km)	Ref.	Minimum size of magma chamber (km^3)[1]	Ref.	Avg. magma composition	Rb conc. (ppm)[2]	Ref.
Porphyry Mo deposits								
Climax	Within-plate	2.2–3.7	1, 2	40–50	21	Rhyolite	500	22
Urad/Henderson (Hideaway Park rhyolite)	Within-plate	1.6–3.1	1, 2, 3	?	22	Rhyolite	380	22
Mt. Emmons + Redwell basin	Within-plate	>(0.7–0.9)	1, 2	?		Rhyolite	270	31
Questa	Within-plate	3–5	4	?		Rhyolite	180	32
Pine Grove	Within-plate	ca. 4	5	100	5	Rhyolite	250	33
Cave Peak	Within-plate	3.0–5.7	6, 7	?		Rhyolite	460	34
Subeconomic Mo mineralization								
Treasure Mountain	Within-plate	ca. 3.7	8, 9	50	23	Rhyolite	320[6]	8
Drammen granite	Within-plate	4.8–5.6	8, 10	60	24	Rhyolite	330	35
Glitrevann granite	Within-plate	>(1.2–1.5)	11	30	25	Rhyolite	160	36
Bear Canyon (Log Cabin prospect)	Within-plate (?)	2–5	12	3	26	Rhyolite	140	32
No economic Mo mineralization								
Rito del Medio pluton	Within-plate (?)	4.1–4.8	13	5	26	Rhyolite	170	32
Canada Pinabete pluton	Subduction (?)	3.5–4.8	13	5	26	Rhyolite	145	32
Stronghold granite	Within-plate (?)	5.6–6.7	6	80	27	Dacite	150 (?)	
Caetano caldera (resurgent plutons)	Subduction	4	14	25	14	Rhyolite	120	14
Tombstone (Schieffelin granodiorite)	Subduction	?		10	28	Dacite	120	37
Porphyry Cu(-Mo, Au) deposits								
Santa Rita	Subduction	>(4.5–4.8)	6	?		Andesite	120	38
Alumbrera	Subduction	>(2.6–4.5)	15, 16	>15	29	Andesite	80	39
Bingham	Subduction	>(3.3–3.5)	17, 18	100–200	30	Dacite	120	30
Butte	Subduction	>(5–9)	19	?		?		
Yerington	Subduction	4–5	20	65	20	Dacite[5]	120	20

References: 1 = Mutschler et al. (1981); 2 = White et al. (1981); 3 = Carten et al. (1988); 4 = Molling (1989); 5 = Keith et al. (1986); 6 = Audétat et al. (2008); 7 = Audétat (2010); 8 = this study; 9 = Everett and Hoisch (2008); 10 = Larsen et al. (2009); 11 = Oftedahl (1978); 12 = Lipman (1988); 13 = Audétat and Pettke (2003); 14 = John et al. (2008); 15 = Ulrich et al. (2002); 16 = Proffett (2003); 17 = Redmond et al. (2004); 18 = Landtwing et al. (2010); 19 = Rusk et al. (2008); 20 = Dilles (1987); 21 = Bookstrom (1989); 22 = Bookstrom et al. (1988); 23 = Mutschler (1976); 24 = Trønnes and Brandon (1992); 25 = Schønwandt and Petersen (1983); 26 = Lipman and Reed (1989); 27 = Drewes (1987); 28 = Moore (1993); 29 = Halter et al. (2005); 30 = Maughan et al. (2002); 31 = Thomas and Galey (1982); 32 = Johnson et al. (1989); 33 = Keith and Shanks (1988); 34 = Price and Henry (1986); 35 = Ihlen et al. (1982); 36 = Jensen (1985); 37 = Lang and Titley (1998); 38 = Audétat and Pettke (2006); 39 = Halter et al. (2004b); 40 = Mutschler (1999); 41 = Keith et al. (1993); 42 = Einaudi (1994)

can be discharged into a confined volume of rock, particularly if an apophysis has developed near the top of the magma chamber. Possibly, this process is aided by a runaway effect: once fractionated melts have gathered under the roof, further fractionation and spatial segregation is promoted due to their reduced viscosity. Shinohara et al. (1995) convincingly demonstrated that once fluid saturation is attained, differences in the density of bubble-bearing vs. undegassed magma can result in efficient magma convection and upward transport of fluids. Importantly, this mechanism works only if the density difference between bubble-bearing and undegassed magma is relatively large, which may be true only at relatively shallow depths. Furthermore, efficient bubble separation at the top of the magma chamber may require the presence of structures through which the volatiles can escape.

In terms of intrusion depth, the Drammen granite (4.8–5.6 km) and the Stronghold granite (5.6–6.7 km) appear to have been emplaced at deeper levels than most porphyry Mo-forming intrusions (2–5 km). In the Drammen granite the occurrence of quartz-topaz greisens in the microcrystalline quartz-feldspar porphyry near Røysjø (Ihlen et al., 1982) and the fact that this rock type is confined to topographically high levels (Trønnes and Brandon, 1992) suggest that the roof was not far. However, in the case of the Stronghold granite, the top of the magma chamber could easily have been situated 1 to 2 km above the present level of erosion, whereas in both cases it is principally possible that economic Mo mineralization was present at structurally higher levels that have already been eroded.

Given the uncertainties outlined above, it may be best to focus on the barely unroofed Treasure Mountain and Glitrevann granites, which were large enough and were emplaced at the right depth to produce economic Mo mineralization, but nevertheless are only subeconomically mineralized. Why were these intrusions not more productive? Although we don't know the ultimate answer, we would like to stress a few points: First, the Treasure Mountain and Glitrevann granites do not seem to have developed the apophyses that are so

Rb, Cs, Mo Concentrations in Barren and Mineralized Intrusions

Cs conc. (ppm)[2]	Ref.	Estimated Mo content (ppm)	Ref.	Estimated total Mo in magma (Mt)	Total Mo in deposit (Mt)	Ref.	Minimum magma volume required to form deposit (km^3)[1]
15	[3]	15	[3]	1.8	2.2	40	110
4	[4]	8	[4]		1.2	40	110
1–5	[3]	3–8	[3]		0.4	40	40–100
4	[4]	7	[4]		0.4	40	40
6	[4]	2	33	0.5	0.2	40	75
18	[4]	12	[4]		0.4	40	25
6	[4]	6	[4]	0.8	n.a.		
1	[4]	6	[4]	1.0	n.a.		
1	[4]	6	[4]	0.5	n.a.		
2	[4]	4	[4]	0.03	0.04	41	7
2	[4]	4	[4]	0.05	–		
3	[4]	4	[4]	0.05	–		
1	[4]	1.5	[4]	0.32	–		
2	14	1.5	[4]	0.10	–		
4.5	37	1.5	[4]	0.04	–		
5	38	2.5	[4]		>0.08	40	>24
1.5	39	4.5	[4]	>0.18	0.3	40	50
–		2[7]		0.5–1.0	0.8	40	300
–		2[7]			1.4	40	500
–		2[7]		0.35	0.04	42	14

[1] See text for details
[2] Minimum Rb and Cs concentrations measured in melt inclusions or whole rocks
[3] Assuming a similar fractionation trend, like the one displayed by melt inclusions from Hideaway Park rhyolite, Treasure Mountain, and the Rito del Medio pluton
[4] Estimated by extrapolating Rb-Cs-Mo trends of melt inclusion data
[5] Luhr Hill granite, 68 wt % SiO_2
[6] Least-evolved melt inclusions, which may not be representative
[7] Estimate based on an average Rb concentration of 120 ppm

characteristic of porphyry Mo-forming intrusions. Also, vent structures, radial dikes, and breccia bodies, which are indicative of forceful ascent of magma and/or fluid, are conspicuously absent in these granites. Instead, miarolitic cavities are common, which testifies to a low degree of fluid focusing. Based on the outcrop situation, it is evident that the roofs of the Treasure Mountain and Glitrevann granites were rather flat. These characteristics are probably related, i.e., the flat roofs may have inhibited apophysis formation and venting, and thus led to poor fluid focusing. Second, the intrusion histories at Treasure Mountain and Glitrevann are comparatively simple, recording only one or, at maximum, two intrusion events, whereas numerous intrusion events are characteristic for porphyry Mo deposits (at least 11 at Henderson [Carten et al., 1988], five at Climax [White et al., 1981], five at Pine Grove [Keith et al., 1986], and at least three at Cave Peak [Sharp, 1978]). Age determinations on separate intrusive phases have shown that magmatic activity lasted for at least 5.5 m.y. (possibly up to 12–15 m.y.) at Climax, and for at least 5 m.y. at Urad-Henderson (White et al., 1981). Such extended lifetimes require repeated reactivation of the magma chamber by melts ascending from depth (Bachmann et al., 2007; Walker et al., 2007). Third, most magmas associated with Climax-type porphyry Mo mineralization show evidence for interaction with mafic alkaline magmas, both in the presence of lamprophyric dikes and mafic enclaves in the felsic intrusions, and in anomalously high Ni and Cr concentrations in the felsic magmas (Bookstrom et al., 1988; Wallace, 1995). Such evidence is mostly missing for the Treasure Mountain and Glitrevann granites. Interaction between mafic and felsic magmas may indirectly be linked to the degree of focusing of residual melts and associated fluids. Bachmann et al. (2007) proposed that magma chambers that are periodically reheated by underplating mafic magmas have a higher chance to develop a cap of fractionated, crystal-poor magma than magma chambers that are not reheated. This crystal-poor cap (see also Miller and Mittlefehldt, 1984; Walker et al., 2007) may be essential for the formation of economic porphyry Mo

mineralization, as the convection model of Shinohara et al. (1995) requires relatively large volumes of crystal-poor magmas at or near aqueous fluid saturation. Magma convection may additionally be facilitated by the high fluorine content of these melts (up to 5 wt %, e.g., White et al., 1981; Wallace, 1995), which adds to the reduction in melt viscosity caused by H_2O (e.g., Baker and Vaillancourt, 1995). How often and in what quantities mafic melts had to arrive for crystal-poor caps to develop, and how important these melts were with regard to providing metals and sulfur (e.g., Keith et al., 1986; Bookstrom et al., 1988; Carten et al., 1993; Audétat, 2010) are not clear at this stage, but helpful information may be obtained by detailed isotopic studies (Bookstrom et al., 1988; Davidson et al., 2007), trace element systematics (e.g., Cr, Ni concentrations in the felsic members; Bookstrom et al., 1988; Keith et al., 1997), and the study of melt inclusions (e.g., Saito et al., 2003; Roberge et al., 2009) and zoned phenocrysts (e.g., Wark et al., 2007).

Summary and Conclusions

Our melt and fluid inclusion study on the subeconomically Mo mineralized granites at Treasure Mountain, Drammen, and Glitrevann has led to the following observations:

1. Molybdenum concentrations in the silicate melt generally increased with increasing degree of fractionation, in the Treasure Mountain dome from ~5 ppm Mo at ~5 ppm Cs to ~35 ppm Mo at ~90 ppm Cs, and in the Drammen granite from ~10 ppm Mo at ~10 ppm Cs to ~30 ppm Mo at ~300 ppm Cs.
2. Magmatic fluids were single phase, had densities between 0.6 and 0.7 g/cm^3, and were of relatively low salinity (~4–6 wt % NaCl equiv). At temperatures ≤600°C these fluids split into a highly saline brine and a coexisting, low-density vapor phase. The single-phase, magmatic fluids contained considerable amounts of S (~0.5 wt % S) and CO_2 (~3–6 mol %).
3. Molybdenum concentrations in these magmatic bulk fluids correlate with Cs concentrations, reflecting the compositional evolution of the silicate melts from which they exsolved. Molybdenum concentrations range from ~50 to ~160 ppm in the Treasure Mountain dome, and from ~30 to ~270 ppm in the Drammen granite.
4. Copper concentrations are poorly reproducible and range from a few tens of ppm to several thousand ppm Cu. The large spread is probably a result of postentrapment diffusion of Cu, but an attempt to reverse these changes resulted in only a relatively small (by a factor of two) decrease in the Cu content of reequilibrated fluid inclusions. In any case, Mo precipitation was highly selective, as the base metal content of the fluids was up to 10 times higher, but there are essentially no base metals in the ore.

Comparison of our melt and fluid inclusion data with previous data obtained from barren intrusions, porphyry Mo-mineralized intrusions, and porphyry Cu (Mo)-mineralized intrusions reveals the following trends:

1. Melts and fluids in subduction-related intrusions were generally less fractionated and had a lower Mo content at a given Cs concentration than melts and fluids analyzed from intrusions in within-plate settings. The latter is in agreement with the lower Mo/Cs ratio of primitive arc magmas relative to oceanic island basalts and suggests that the molybdenum in both subduction-related and within-plate magmas is mantle derived.
2. Fluids and melts in barren and subeconomically mineralized intrusions from within-plate settings lie on the same fractionation trends as those analyzed from economic porphyry Mo deposits.

This shows that the fluids and melts that were present at high degrees of crystallinity in barren intrusions were not fundamentally different from those that formed giant porphyry Mo deposits. The difference must have been either the magma volumes or the degree of focusing of fractionated melts and exsolved fluids thereof. Based on the available data, it can be calculated that at least several tens of km^3 magma were required to form intermediate to large deposits, and at least several hundred km^3 of magma to form giant deposits. Hence, some of the barren intrusions may have been simply too small to produce major Mo mineralization. However, other intrusions, including the Treasure Mountain dome and the Drammen and Glitrevann granites, would have had the required size. In these intrusions the lack of economic mineralization seems to be the result of poor focusing of residual melts and fluids. Apophyses, vent structures, and breccia bodies are conspicuously absent in these intrusions. Instead, miarolitic cavities are present, testifying to a dispersed state of the fluids. There is little doubt that the presence of apophyses with overlying areas of highly fractured rocks is a critical requirement for focused fluid flow. Furthermore, the enormous amounts of Mo present in some deposits (>1 Mt Mo) associated with small (<0.5 km^3) apophyses require that magma was very efficiently circulated through these apophyses (Shinohara et al., 1995). Which factors ultimately lead to the accumulation of large volumes of fractionated melts in the upper parts of magma chambers and how these factors are related to the tectonic framework are less clear. Potential factors include the intrinsic properties of the intruding magmas, the rate and depth of magma intrusion, and the degree of interaction with mafic magmas.

Acknowledgments

This work was funded by the German Science Foundation under project number AU 314/1-2. We thank Ronald Bakker, who provided assistance with using the ICE software, Celestine Mercer for the data from the Hideaway Park rhyolite, and Hans Keppler for additional funding and for help with the Raman spectroscopy. Furthermore, we would like to thank Gleb Pokrovski, Anastassia Borisova, and an anonymous reviewer for their constructive comments.

REFERENCES

Audétat, A., 2010, Source and evolution of molybdenum in the porphyry Mo(-Nb) deposit at Cave Peak, Texas: Journal of Petrology, v. 51, p. 1739–1760.

Audétat, A., and Lowenstern, J.B., 2012, Melt inclusions, *in* Scott, S.D., ed., Geochemistry of mineral resources, Treatise on geochemistry, v. 12: Oxford, Elsevier-Pergamon, in press.

Audétat, A., and Pettke, T., 2003, The magmatic-hydrothermal evolution of two barren granites: A melt and fluid inclusion study of the Rio del Medio

and Cañada Pinabete plutons in northern New Mexico (USA): Geochimica et Cosmochimica Acta, v. 67, p. 91–121.

——2006, Evolution of a porphyry-Cu mineralized magma system at Santa Rita, New Mexico (USA): Journal of Petrology, v. 47, p. 2021–2046.

Audétat, A., Pettke, T., and Dolejš, D., 2004, Magmatic anhydrite and calcite in the ore-forming quartz-monzodiorite magma at Santa Rita, New Mexico (USA): Genetic constraints on porphyry-Cu mineralization: Lithos, v. 72, p. 147–161.

Audétat, A., Pettke, T., Heinrich, C.A., and Bodnar, R.J., 2008, The composition of magmatic-hydrothermal fluids in barren and mineralized intrusions: Economic Geology, v. 103, p. 877–908.

Audétat, A., Dolejs, D., and Lowenstern, J.B., 2011, Molybdenite saturation in silicic magmas: Occurrence and petrological implications: Journal of Petrology, v. 52, p. 891–904.

Bachmann, O., Miller, C.F., and de Silva, S.L., 2007, The volcanic-plutonic connection as a stage for understanding crustal magmatism: Journal of Volcanology and Geothermal Research, v. 167, p. 1–23.

Baker, D.R., and Vaillancourt, J., 1995, The low viscosities of F+H_2O-bearing granitic melts and implications for melt extraction and transport: Earth and Planetary Science Letters, v. 132, p. 199–211.

Bakker, R.J., 1997, Clathrates: Computer programs to calculate fluid inclusion V-X properties using clathrate melting temperatures: Computers & Geosciences, v. 23, p. 1–18.

Bali, E., Keppler, H., and Audétat, A., 2012, The mobility of W and Mo in subduction zone fluids and the Mo-W-Th-U systematics of island arc magmas: Earth and Planetary Science Letters, v. 351–352, p. 195–207.

Berthelsen, A., 1980, Towards a palinspastic tectonic analysis of the Baltic Shield: 26th International Geological Congress, Paris, Memoires du Bureau de Recherches Géologiques et Minières (B.R.G.M.), v. 108, p. 5–21.

Bodnar, R.J., and Student, J.J., 2006, Melt inclusions in plutonic rocks: Petrography and microthermometry: Mineralogical Association of Canada, Short Course Series, v. 36, p. 1–26.

Bodnar, R.J., and Vityk, M.O., 1994, Interpretation of microthermometric data for H_2O-NaCl fluid inclusions: Blacksburg, VA, Virginia Tech, p. 117–130.

Bookstrom, A.A., 1989, The Climax-Alma granite batholith of Oligocene age and the porphyry molybdenum deposits of Climax, Colorado, U.S.A.: Engineering Geology, v. 27, p. 543–568.

Bookstrom, A.A., Carten, R.B., Shannon, R.D., and Smith, R.P., 1988, Origins of bimodal leucogranite-lamprophyre suites, Climax and Red Mountain porphyry molybdenum systems, Colorado: Petrologic and strontium isotopic evidence: Colorado School of Mines Quarterly, v. 83, p. 1–65.

Borisova, A.Y., Freydier, R., Polvé, M., Salvi, S., Candaudap, F., and Aigouy, T., 2008, In situ multi-element analysis of the Mount Pinatubo quartz-hosted melt inclusions by NIR femtosecond laser ablation-inductively coupled plasma-mass spectrometry: Geostandards and Geoanalytical Research, v. 32, p. 209–229.

Bugge, A., 1963, Norges molybdenforekomster: Norges Geologiske Undersokelse, v. 259, p. 65–84.

Burke, W.A.J., 2001, Raman microspectrometry of fluid inclusions: Lithos, v. 55, p. 139–158.

Carten, R.B., Geraghty, E.P., and Walker, B.M., 1988, Cyclic development of igneous features and their relationship to high-temperature hydrothermal features in the Henderson porphyry molybdenum deposit, Colorado: Economic Geology, v. 83, p. 266–296.

Carten, R.B., White, W.H. and Stein, H.J., 1993, High-grade granite-related molybdenum systems: Classification and origin: Geological Association of Canada, Special Paper 40, p. 521–554.

Clark, K.F., and Read, C.B., 1972, Geology and ore deposits of the Eagle Nest area, New Mexico: New Mexico Bureau of Mines and Mineral Resources Bulletin, v. 94, 152 p.

Davidson, J.P., Morgan, D.J., Charlier, B.L.A., Harlou, R., and Hora, J.M., 2007, Microsampling and isotopic analysis of igneous rocks: Implications for the study of magmatic systems: Annual Review of Earth and Planetary Science Letters, v. 35, p. 273–311.

Dilles, J.H., 1987, Petrology of the Yerington batholith, Nevada: Evidence for evolution of porphyry copper ore fluids: Economic Geology, v. 82, p. 1750–1789.

Drewes, H., 1987, Geologic map and cross sections of the Dragoon Mountains, southeastern Arizona: U.S. Geological Survey Miscellaneous Investigations Series, Map I-1662.

Einaudi, M.T., 1994, 6-km vertical cross section through porphyry copper deposits, Yerington district, Nevada: Multiple intrusions, fluids, and metal sources: Society of Economic Geologists, International Exchange Lecture, June 1994, http://pangea.stanford.edu/research/ODEX/marco-yerington.html.

Everett, B.C., and Hoisch, T.D., 2008, Conditions of metamorphism of the Colorado Yule Marble: Mountain Geologist, v. 45, p. 69–76.

Geyti, A., and Schønwandt, H.K., 1979, Bordvika—a possible porphyry molybdenum occurrence within the Oslo rift, Norway: Economic Geology, v. 74, p. 1211–1220.

Guillong, M., and Heinrich, C.A., 2007, Sensitivity enhancement in laser ablation ICP-MS using small amounts of hydrogen in the carrier gas: Journal of Analytical Atomic Spectrometry, v. 22, p. 1488–1494.

Halter, W.E., Pettke, T., and Heinrich, C.A., 2004a, Laser-ablation ICP-MS analysis of silicate melt and sulfide melt inclusions in an andesitic complex I: Analytical approach and data evaluation: Contributions to Mineralogy and Petrology, v. 147, p. 385–396.

Halter, W.E., Heinrich, C.A., and Pettke, T., 2004b, Laser-ablation ICP-MS analysis of silicate and sulfide melt inclusions in an andesitic complex; II, Evidence for magma mixing and magma chamber evolution: Contributions to Mineralogy and Petrology, v. 147, p. 397–412.

——2005, Magma evolution and the formation of porphyry Cu-Au ore fluids: Evidence from silicate and sulfide melt inclusions: Mineralium Deposita, v. 39, p. 845–863.

Hedenquist, J.W., and Henley, R.W., 1985, The importance of CO_2 on freezing point measurements of fluid inclusions: Evidence from active geothermal systems and implications for epithermal ore deposition: Economic Geology, v. 80, p. 1379–1406.

Heinrich, C.A., Pettke, T., Halter, W.E., Aigner-Torres, M., Audétat, A., Günther, D., Hattendorf, B., Bleiner, D., Guillong, M., and Horn, I., 2003, Quantitative multi-element analysis of minerals, fluid and melt inclusions by laser-ablation inductively-coupled-plasma mass-spectrometry: Geochimica et Cosmochimica Acta, v. 67, p. 3473–3496.

Holtz, F., Johannes, W., Tamic, N., and Behrens, H., 2001, Maximum and minimum water contents of granitic melts generated in the crust: A reevaluation and implications: Lithos, v. 56, p. 1–14.

Ihlen, P.M., 1986, The geological evolution and metallogeny of the Oslo paleorift, *in* Olerud, S., and Ihlen, P.M., eds., Metallogeny associated with the Oslo paleorift: Uppsala, Sveriges Geologiska Undersökning, p. 6–17.

Ihlen, P.M., and Vokes, F.M., 1978, Metallogeny: Bulletin-Norges Geologiske Undersokelse, v. 45, p. 75–90.

Ihlen, P.M., Tronnes, R.G., and Vokes, F.M., 1982, Mineralization, wall rock alteration and zonation of ore deposits associated with the Drammen granite in the Oslo region, Norway, *in* Evans, A.M., ed., Metallization associated with acid magmatism: Chichester, John Wiley & Sons Ltd, p. 111–136.

Jensen, I.S., 1985, Geochemistry of the central granitic stock in the Glitrevann cauldron within the Oslo rift, Norway: Norsk Geologisk Tidsskrift, v. 65, p. 201–216.

John, D.A., Henry, C.D., and Colgan, J.P., 2008, Magmatic and tectonic evolution of the Caetano caldera, north-central Nevada; a tilted, mid-Tertiary eruptive center and source of the Caetano Tuff: Geosphere, v. 4, p. 75–106.

Johnson, C.M., Czamanske, G.K., and Lipman, P.W., 1989, Geochemistry of intrusive rocks associated with the Latir volcanic field, New Mexico, and contrasts between evolution of plutonic and volcanic rocks: Contributions to Mineralogy and Petrology, v. 103, p. 90–109.

Jones, D.M., 1990, Mid-tertiary arcuate dikes and faults of the Rio Hondo-Red River drainages, Sangre de Cristo Mountains, New Mexico: A postulated outlying ring-fracture zone to the Miocene Questa caldera: New Mexico Geological Society Guidebook, 41st Field Conference, p. 365–368.

Kamenetsky, V.S., and Danyushevsky, L.V., 2005, Metals in quartz-hosted melt inclusions: Natural facts and experimental artifacts: American Mineralogist, v. 90, p. 1674–1678.

Keith, J.D., and Shanks, W.C., 1988, Chemical evolution and volatile fugacities of the Pine Grove porphyry molybdenum and ash-flow tuff system, southwest Utah, *in* Taylor, R.P., and Strong, D.F., eds., Recent advances in the geology of granite-related mineral deposits: Canadian Institute of Mining and Metallurgy Special Volume, p. 402–423.

Keith, J.D., Shanks, W.C., Archibald, D.A., and Ferrar, E., 1986, Volcanic and intrusive history of the Pine Grove porphyry molybdenum system, southwestern Utah: Economic Geology, v. 81, p. 553–577.

Keith, J.D., Christiansen, E.H., and Carten, R.B., 1993, The genesis of giant porphyry molybdenum deposits: Society of Economic Geologists Special Publication, v. 2, p. 285–317.

Keith, J.D., Whitney, J.A., Hattori, K., Ballantyne, G.H., Christiansen, E.H., Barr, D.L., Cannan, T.M., and Hook, C.J., 1997, The role of magmatic

sulfides and mafic alkaline magmas in the Bingham and Tintic mining districts, Utah: Journal of Petrology, v. 38, p. 1679–1690.

Klemm, L.M., Pettke, T., Heinrich, C.A., and Campos, E., 2007, Hydrothermal evolution of the El Teniente deposit, Chile: Porphyry Cu-Mo ore deposition from low-salinity magmatic fluids: Economic Geology, v. 102, p. 1021–1045.

Klemm, L.M., Pettke, T., and Heinrich, C.A., 2008, Fluid and source magma evolution of the Questa porphyry Mo deposit, New Mexico, USA: Mineralium Deposita, v. 43, p. 533–552.

Landtwing, M.R., Furrer, C., Redmond, P.B., Pettke, T., Guillong, M., and Heinrich, C.A., 2010, The Bingham porphyry Cu-Mo-Au deposit. III. Zoned copper-gold ore deposition by magmatic vapor expansion: Economic Geology, v. 105, p. 91–118.

Lang, J.R., and Titley, S.R., 1998, Isotopic and geochemical characteristics of Laramide magmatic systems in Arizona and implications for the genesis of porphyry copper deposits: Economic Geology, v. 93, p. 138–170.

Larsen, R.B., Jacamon, F., and Kronz, A., 2009, Trace element chemistry and textures of quartz during the magmatic hydrothermal transition of Oslo rift granites: Mineralogical Magazine, v. 73, p. 691–707.

Lehmann, B., 1987, Molybdenum distribution in Precambrian rocks of the Colorado mineral belt: Mineralium Deposita, v. 22, p. 47–52.

Lerchbaumer, L., and Audétat, A., 2012a, The 'quartz capsule'—a new method to avoid alloying problems with noble metal capsules in hydrothermal experiments: European Journal of Mineralogy, v. 24, p. 683–693.

——2012b, High Cu concentrations in vapor-type fluid inclusions: An artifact?: Geochimica et Cosmochimica Acta, v. 88, p. 255–274.

Li, Y., Audétat, A., Lerchbaumer, L., and Xiong, X.L., 2009, Rapid Na, Cu exchange between synthetic fluid inclusions and external aqueous solutions: Evidence from LA-ICP-MS analysis: Geofluids, v. 9, p. 321–329.

Lipman, P.W., 1988, Evolution of silicic magma in the upper crust; the mid-Tertiary Latir volcanic field and its cogenetic granitic batholith, northern New Mexico, U.S.A.: Transactions of the Royal Society of Edinburgh: Earth Sciences, v. 79, p. 265–288.

Lipman, P.W., and Reed, J.C., 1989, Geologic map of the Latir volcanic field and adjacent areas, northern New Mexico: U.S. Geological Survey Miscellaneous Investigations Series, Map I-1907.

Lowenstern, J.B., 1994, Dissolved volatile concentrations in an ore-forming magma: Geology, v. 22, p. 893–896.

Maughan, D.T., Keith, J.D., Christiansen, E.H., Pulsipher, T., Hattori, K., and Evans, N.J., 2002, Contributions from mafic alkaline magmas to the Bingham porphyry Cu-Au-Mo deposit, Utah, USA: Mineralium Deposita, v. 37, p. 14–37.

Mavrogenes, J.A., and Bodnar, R.J., 1994, Hydrogen movement into and out of fluid inclusions in quartz: Experimental evidence and geologic implications: Geochimica et Cosmochimica Acta, v. 58, p. 141–149.

Miller, C.F., and Mittlefehldt, D.W., 1984, Extreme fractionation in felsic magma chambers; a product of liquid-state diffusion or fractional crystallization?: Earth and Planetary Science Letters, v. 68, p. 151–158.

Molling, P.A., 1989, Applications of the reaction progress variable to hydrothermal alteration associated with the deposition of the Questa molybdenite deposit, NM: Unpublished Ph.D. thesis, Baltimore, Johns Hopkins University, 249 p.

Moore, R.B., 1993, Geologic map of the Tombstone volcanic center, Cochise County, Arizona: U.S. Geological Survey Miscellaneous Investigations Series, Map I-2420.

Mutschler, F.E., 1976, Crystallization of a soda granite, Treasure Mountain dome, Colorado, and the genesis of stockwork molybdenite deposits, *in* Woodward, L.A., and Northrop, S.A., eds., Tectonics and mineral resources of southwestern North America: New Mexico Geological Society Special Publication, p. 199–205.

Mutschler, F.E., Rougon, D.J., and Lavin, O.P., 1976, PETROS, a data bank of major-element chemical analyses of igneous rocks for research and teaching: Computers and Geosciences, v. 2, p. 51–57. (an update dating from 1980 can be downloaded at http://www.ngdc.noaa.gov/mgg/geology/petros.html)

Mutschler, F.E., Wright, E.G., Ludington, S., and Abbott, J.T., 1981, Granite molybdenite systems: Economic Geology, v. 76, p. 874–897.

Mutschler, F.E., Ludington, S.D., and Bookstrom, A.A., 1999, Giant porphyry-related metal camps of the world; a database: U.S. Geological Survey Open File Report 99-556, http://pubs.usgs.gov/of/1999/of99-556/.

Neumann, E.-R., Olsen, K.I., Baldridge, W.S., and Sundvoll, B., 1992, The Oslo rift: A review: Tectonophysics, v. 208, p. 1–18.

Obradovich, J.D., Mutschler, F.E., and Bryant, B., 1969, Potassium-argon ages bearing on the igneous and tectonic history of the Elk Mountains and vicinity, Colorado: A preliminary report: Geological Society of America Bulletin, v. 80, p. 1749–1756.

Oftedahl, C., 1953, Studies on the igneous rock complex of the Oslo region. XIII. The cauldrons: Skrifter-Norske Videnskaps-Akademi i Oslo, I. Matematisk-Naturvidenskapelig Klasse, v. 3, p. 108.

——1978, Cauldrons of the Permian Oslo rift: Journal of Volcanology and Geothermal Research, v. 3, p. 343–371.

Olsen, K.I., and Griffin, W.L., 1984, Fluid inclusion studies of the Drammen granite, Oslo Paleorift, Norway. I. Microthermometry: Contributions to Mineralogy and Petrology, v. 87, p. 1–14.

Peng, D.Y., and Robinson, D.B., 1976, A new two-constant equation of state: Industrial and Engineering Chemistry Fundamentals, v. 15, p. 59–64.

Pettke, T., 2006, In-situ laser-ablation-ICP-MS chemical analysis of melt inclusion and prospects for constraining subduction zone magmas: Mineralogical Association of Canada (MAC) Short Course Series, v. 36, p. 51–80.

Pettke, T., Oberli, F., and Heinrich, C.A., 2010, The magma and metal source of giant porphyry-type ore deposits, based on lead isotope microanalysis of individual fluid inclusions: Earth and Planetary Science Letters, v. 296, p. 267–277.

Price, J.G., and Henry, C.D., 1986, Geology of Marble Canyon: University of Texas at Austin, Guidebook-Bureau of Economic Geology, v. 23, p. 17–26.

Proffett, J.M., 2003, Geology of the Bajo de la Alumbrera porphyry copper-gold deposit, Argentina: Economic Geology, v. 98, p. 1535–1574.

Ramberg, I.B., Gabrielsen, R.H., Larsen, B.T., and Solli, A., 1977, Analysis of fracture patterns in southern Norway: Geologie en Mijnbouw, Netherlands Journal of Geosciences, v. 56, p. 295–310.

Redmond, P.B., Einaudi, M.T., Inan, E.E., Landtwing, M.R., and Heinrich, C.A., 2004, Copper deposition by fluid cooling in intrusion-centered systems: New insights from the Bingham porphyry ore deposit, Utah: Geology, v. 32, p. 217–220.

Richards, J.P., 2011, Magmatic to hydrothermal metal fluxes in convergent and collided margins: Ore Geology Reviews, v. 40, p. 1–26.

Roberge, J., Delgado-Granados, H., and Wallace, P.J., 2009, Mafic magma recharge supplies high CO_2 and SO_2 gas fluxes from Popocatépetl volcano, Mexico: Geology, v. 37, p. 107–110.

Roedder, E., 1984, Fluid inclusions: Reviews in Mineralogy, v. 12, 644 p.

Rudnick, R.L., and Gao, S., 2003, The composition of the continental crust, *in* Holland, H.D., and Turekian, K.K. eds., The crust, Treatise on geochemistry: Oxford, Elsevier-Pergamon, v. 3, p. 1–64.

Rusk, B.D., Reed, M.H., Dilles, J.H., Klemm, L.M., and Heinrich, C.A., 2004, Compositions of magmatic hydrothermal fluids determined by LA-ICP-MS of fluid inclusions from the porphyry copper-molybdenum deposit at Butte, MT: Chemical Geology, v. 210, p. 173–199.

Rusk, B.D., Reed, M.H., and Dilles, J.H., 2008, Fluid inclusion evidence for magmatic-hydrothermal fluid evolution in the porphyry copper-molybdenum deposit at Butte, Montana: Economic Geology, v. 103, p. 307–334.

Saito, G., Kazahaya, K., and Shinohara, H., 2003, Volatile evolution of Satsuma-Iwojima volcano: Degassing process and mafic-felsic magma interaction, *in* DeVivo, B., and Bodnar, R.J., eds., Melt inclusions in volcanic systems: Elsevier, p. 129–146.

Schmidt, C., and Bodnar, R. J., 2000, Synthetic fluid inclusions: XVI. PVTX properties in the system H_2O-NaCl-CO_2 at elevated temperatures, pressures, and salinities: Geochimica et Cosmochimica Acta, v. 64, p. 3853–3869.

Schønwandt, H.K., 1986, The volcanic history and the molybdenite mineralization of the Glitrevann caldera: Uppsala, Sveriges Geologiska Undersökning, v. 59, p. 26–27.

Schønwandt, H.K., and Petersen, J.S., 1983, Continental rifting and porphyry-molybdenum occurrences in the Oslo region, Norway: Tectonophysics, v. 94, p. 609–631.

Seedorff, E., Dilles, J.H., Proffett, J.M.J., Einaudi, M.T., Zurcher, L., Stavast, W.J.A., Johnson, D.A., and Barton, M.C., 2005, Porphyry deposits: Characteristics and origin of hypogene features: Economic Geology 100th Anniversary Volume, p. 251–298.

Seo, J.H., Guillong, M., and Heinrich, C.A., 2009, The role of sulfur in the formation of magmatic-hydrothermal copper-gold deposits: Earth and Planetary Science Letters, v. 282, p. 323–328.

Seo, J.H., Guillong, M., Aerts, M., Zajacz, Z., and Heinrich, C.A., 2011, Microanalysis of S, Cl, and Br in fluid inclusions by LA-ICP-MS: Chemical Geology, v. 284, p. 35–44.

Seo, J.H., Guillong, M., and Heinrich, C.A., 2012, Separation of molybdenum and copper in porphyry deposits: The roles of sulfur, redox, and pH in ore mineral deposition at Bingham Canyon: Economic Geology, v. 107, p. 333–356.

Sharp, J.E., 1978, A molybdenum mineralized breccia pipe complex, Redwell basin, Colorado: Economic Geology, v. 73, p. 369–382.

Shinohara, H., Kasahaya, K., and Lowenstern, J.B., 1995, Volatile transport in a convecting magma column: Implications for porphyry Mo mineralization: Geology, v. 23, p. 1091–1094.

Sillitoe, R.H., 2010, Porphyry copper systems: Economic Geology, v. 105, p. 3–41.

Sinclair, W.D., 2007, Porphyry deposits, *in* Goodfellow, W.D., ed., Mineral deposits of Canada: A synthesis of major deposit-types, district metallogeny, the evolution of geological provinces, and exploration methods: Geological Association of Canada, Mineral Deposits Division, Special Publication, p. 223–243.

Skjernaa, L., and Pedersen, S., 1982, The effect of penetrative Sveconorwegian deformation on the Rb-Sr isotopic systems in the Rømskog-Aurskog-Høland area, SE Norway: Precambrian Research, v. 17, p. 215–243.

Spandler, C., Pettke, T., and Rubatto, D., 2011, Internal and external fluid sources for eclogite-facies veins in the Monviso meta-ophiolite, Western Alps; implications for fluid flow in subduction zones: Journal of Petrology, v. 52, p. 1207–1236.

Starmer, I.C., 1972, The Sveconorwegian regeneration and earlier orogenetic events in the Bamble series, south Norway: Norges Geologiske Undersokelse, v. 277, p. 37–52.

——1985a, The evolution of the south Norwegian Proterozoic as revealed by the major and mega-tectonics of the Kongsberg and Bamble sectors: NATO Advanced Study Institutes Series, Series C: Mathematical and Physical Sciences, p. 259–290.

——1985b, The geology of the Kongsberg district and the evolution of the entire Kongsberg sector, south Norway: Norges Geologiske Undersokelse, v. 401, p. 35–58.

Sun, S.S., and McDonough, W.F., 1989, Chemical and isotopic systematics of oceanic basalts: Implications for mantle composition and processes, *in* Saunders, A.D., and Norry, M.J., eds., Magmatism in the ocean basins: London, Geological Society, Special Publications, p. 313–345.

Sundvoll, B., and Larsen, B.T., 1982, Datings of major geological stress indicators in the development of a rift system: The Oslo paleorift: Terra Cogita, v. 2, p. 64.

——1990, Rb-Sr isotope systematics in the magmatic rocks of the Oslo rift: Norges Geologiske Undersokelse, v. 418, p. 27–46.

Sundvoll, B., Larsen, B.T., and Wandaas, B., 1992, Early magmatic phase in the Oslo rift and its related stress regime: Tectonophysics, v. 208, p. 1–3.

Taylor, S.R., 1964, Abundance of chemical elements in the continental crust: A new table: Geochimica et Cosmochimica Acta, v. 28, p. 1273–1285.

Thomas, J.A., and Galey, J.T., 1982, Exploration and geology of the Mt. Emmons molybdenite deposits, Gunnison County, Colorado: Economic Geology, v. 77, p. 1085–1104.

Trønnes, R.G., and Brandon, A.D., 1992, Mildly peraluminous high-silica granites in a continental rift: The Drammen and Finnemarka batholiths, Oslo rift, Norway: Contributions to Mineralogy and Petrology, v. 109, p. 275–294.

Tweto, O., and Sims, P.K., 1963, Precambrian ancestry of the Colorado mineral belt: Geological Society of America Bulletin, v. 74, p. 991–1014.

Ulrich, T., Günther, D., and Heinrich, C.A., 2002, The evolution of a porphyry Cu-Au deposit, based on LA-ICP-MS analysis of fluid inclusions: Bajo de la Alumbrera, Argentina: Economic Geology, v. 97, p. 1889–1920.

Walker, B.A., Miller, C.F., Lowery Claiborne, L., Wooden, J.L., and Miller, J.S., 2007, Geology and geochronology of the Spirit Mountain batholith, southern Nevada: Implications for timescales and physical processes of batholith construction: Journal of Volcanology and Geothermal Research, v. 167, p. 239–262.

Wallace, S.R., 1995, The Climax-type molybdenum deposits—What they are, where they are, and why they are: Economic Geology, v. 90, p. 1359–1380.

Wallace, S.R., Muncaster, N.K., Johnson, D.C., MacKenzie, W.B., Bookstrom, A.A., and Surface, V.E., 1968, Multiple intrusion and mineralization at Climax, Colorado: American Institute of Mining, Metallurgical, and Petroleum Engineers (A.I.M.E.) Graton-Sales Volume, p. 605–640.

Wareham, C.D., Rice, C.M., Boyce, A.J., and Rogers, G., 1998, S, C, Sr, and Pb sources in the Pliocene Silver Creek porphyry Mo system, Rice, Colorado: Economic Geology, v. 93, p. 32–46.

Wark, D.A., Hildreth, W., Spear, F.S., Cherniak, D.J., and Watson, E.B., 2007, Pre-eruption recharge of the Bishop magma system: Geology, v. 35, p. 235–238.

Watson, B.E., and Harrison, M.T., 1983, Zircon saturation revisited: Temperature and composition effects in a variety of crystal magma types: Earth and Planetary Science Letters, v. 64, p. 295–304.

Westra, G., and Keith, S.B., 1981, Classification and genesis of stockwork molybdenum deposits: Economic Geology, v. 76, p. 844–873.

White, W.H., Bookstrom, A.A., Kamilli, R.J., Ganster, M.W., Smith, R.P., Ranta, D.E., and Steininger, R.C., 1981, Character and origin of Climax-type molybdenum deposits: Economic Geology 75th Anniversary Volume, p. 270–316.

Zajacz, Z., Halter, W.E., Pettke, T., and Guillong, M., 2008, Determination of fluid/melt partition coefficients by LA-ICP-MS analysis of co-existing fluid and silicate melt inclusions: Controls on element partitioning: Geochimica et Cosmochimica Acta, v. 72, p. 2169–2197.

Zajacz, Z., Hanley, J.J., Heinrich, C.A., Halter, W.E., and Guillong, M., 2009, Diffusive reequilibration of quartz-hosted silicate melt and fluid inclusions: Are all metal concentrations unmodified?: Geochimica et Cosmochimica Acta, v. 73, p. 3013–3027.

Zhang, L., Audétat, A., and Dolejs, D., 2012, Solubility of molybdenite (MoS_2) in aqueous fluids at 600–800 °C, 200 MPa: A synthetic fluid inclusion study: Geochimica et Cosmochimica Acta, v. 77, p. 175–185.